JOURNAL OF GEOPHYSICAL RESEARCH, VOL. 102, NO. E1, PAGES 1613–1635, JANUARY 25, 1997

The interior structure of Mars: Implications from SNC meteorites

Frank Sohl and Tilman Spohn

Institut für Planetologie, Westfälische Wilhelms-Universität, Münster, Germany

Abstract. Two end–member models of Mars' present interior structure are presented: the first model is optimized to satisfy the geochemical data derived from the SNC meteorites in terms of the bulk chondritic ratio Fe/Si = 1.71, while the second model is optimized to satisfy the most probable maximum value $C = 0.366 \times M_p r_p^2$ of the polar moment of inertia factor. Hydrostatic equilibrium and stationary heat transfer are assumed, and the basic differential equations for the mechanical and thermal structure are solved numerically together with an isothermal Murnaghan–Birch type equation of state truncated in Eulerian strain at forth order. We obtain the radial distribution of mass, hydrostatic pressure, gravity, temperature, and heat flow density along with the corresponding density stratification, viscosity profiles, and the global seismic velocity structure of model Mars. The first model being consistent with the geochemical requirement produces $C = 0.357 \times M_p r_p^2$, whereas the second model commensurate with the geophysical constraint gives Fe/Si = 1.35. The calculated central pressure is about 40 GPa in both models, and the central temperature is in the 2000 to 2200 K range. The model calculations suggest a Fe-Ni–FeS core a little less than one half of the planetary radius in size surrounded by a silicate mantle subdivided into lower spinel and upper olivine layers and overlain by a 100- to 250-km thick basaltic crust and a surface heatflow density of 25 to 30 mW m^{-2}. In both models the pressure in the mantle is not sufficient for the spinel to perovskite transition to occur. The present thermal lithosphere is estimated to be about 500 km thick and to be subdivided into a 300-km-thick outermost rheological lithosphere and an underlying thermal boundary layer of mantle convection. Given the core sulfur content of 14 wt% as derived from SNC meteorites, the Martian core is found to be entirely molten, implying the nonoperation of a self–sustained dynamo due to the absence of sufficiently vigorous convection.

Introduction

Interior models for the planet Mars continue to be of interest as the drive for deeper exploration of the red planet gains momentum. The next decade will see a suite of missions to Mars launched by NASA, and possibly, by the European Space Agency (ESA). If all goes well, seismometers will soon be placed on the surface of Mars and provide unprecedented opportunities for exploring the planet's interior structure and activity. In the meantime, models of the Martian interior are constrained by the gravity field and by cosmochemical data derived from the SNC (Shergotty, Nakhla, and Chassigny) meteorites and from the comparatively old, cumulate orthopyroxenite meteorite ALH84001, which are widely believed to come from Mars. The close relationship of the latter to the SNCs was recognized recently from petrographic and isotopic evidence [*Mittlefehldt*, 1994]. Because of their young internal crystallisation ages of less than 1.3 Gyr and basaltic to ultramafic compositions, the members of the SNC suite are believed to have been ejected from the less cratered, young terrains of the northern lowlands in one or several impact events. In contrast, ALH84001 was subjected to at least two shock deformation events, thermal metamorphism, and aqueous alteration and probably represents old igneous crustal rock of Hesperian or Noachian age sampled during a separate impact in the southern highlands [*McSween*, 1985,1994; *Treiman*, 1995; *Ash et al.*, 1996] .

Prior to the exploration of Mars by space probes such as the Vikings, attempts at modeling the interior structure of the planet suffered from poorly known values of its radius and moment of inertia [e.g., *Urey*, 1952]. Improved measurements of the planet's mass M_p, radius r_p, gravitational potential, and rotation rate by Mariner and Viking provided the geodetical constraints required for models of the interior structure [*Born*, 1974; *Bills and Ferrari*, 1978; *Balmino et al.*, 1982]. Unfortu-

Paper number 96JE03419.
0148-0227/97/96JE-03419$09.00

nately, the most important constraint on the concentration of mass toward the center, the planet's polar principal moment of inertia C, is still poorly known. Until the precession period of the spin axis of Mars is determined, estimates of C suffer from assumptions about the magnitudes of the nonhydrostatic contributions, in particular those of the Tharsis rise, to the oblateness of the Martian gravitational potential. Assuming that Mars is in a hydrostatic state, $C = 0.376 \times M_p r_p^2$ is calculated from the observed gravitational oblateness J_2 [*Cook*, 1977]. Accounting for nonhydrostatic contributions by assuming an axisymmetric distribution of topographic loads about Tharsis yields the generally prefered value of $C = 0.365 \times M_p r_p^2$ [*Reasenberg*, 1977; *Kaula*, 1979]. *Bills* [1989], however, has pointed out that the assumption of axial symmetry provides an upper limit to the corrected value of C, since the nonhydrostatic component is certainly three dimensional. If the nonhydrostatic contribution to J_2 is a maximally triaxial ellipsoid (intermediate axis nearly midway between the greatest and smallest axis) as suggested by *Bills* [1989], then $C = 0.345 \times M_p r_p^2$, which provides a lower bound on realistic values for C.

Early compositional and structural models of Mars have used the hydrostatic value of $C = 0.376 \times M_p r_p^2$ [*Binder*, 1969; *Anderson*, 1972; *Binder and Davis*, 1973; *Johnston et al.*, 1974]. More recent models used $C = 0.365 \times M_p r_p^2$ [*Johnston and Toksöz*, 1977; *McGetchin and Smyth*, 1978; *Okal and Anderson*, 1978; *Morgan and Anders*, 1979; *Göttel*, 1981; *Schubert and Spohn*, 1990; *Ohtani and Kamaya*, 1992] and obtained larger core size estimates and generally less dense but still FeO-rich mantle compositions. In general, these models have core radii around $0.5 r_p$, mantle densities of (3440 ± 60) kg m^{-3} corresponding to a FeO content of 15 wt% and core mass fractions between 14.8% (pure iron) and 26.3% (pure troilite) [*Göttel*, 1981]. *Schubert and Spohn* [1990] have varied $C/M_p r_p^2$ between 0.345 and 0.365 and find that the lower bound would require unrealistically low values of the mantle density.

Structural models based on chemical arguments show similar variations in core size estimates. It has been suggested that the addition of about 13 wt% FeO to terrestrial pyrolite could explain the relatively large mantle density required to satisfy $C/M_p r_p^2 = 0.365$. This composition of the Martian mantle would allow for ultrabasic mantle-derived partial melts of low viscosity [*McGetchin and Smyth*, 1978]. A similar chemical composition of Mars has been calculated by *Morgan and Anders* [1979] using a chondritic bulk iron content of 26.7 wt% and some key element abundances representing fractionation processes in the early solar system. This model has a core mass fraction of 19%. From recent considerations of element correlations in SNC meteorites and cosmochemical constraints [*Wänke and Dreibus*, 1988], the Martian interior has been concluded to be composed of a highly reduced refractory component and an oxydized volatile-rich one. According to these data, Mars is differentiated into a FeO-rich silicate mantle containing radiogenic heat sources in terrestrial abundances and a sulfur-rich Fe-Ni-FeS core of about 22% of the planet's mass and a core radius of $0.5 r_p$. The model is predicated on a global Fe/Si ratio of 1.71 representative of the composition of carbonaceous chondrites. Converting the mantle composition of *Dreibus and Wänke* [1985] into a pressure-dependent mineralogy, *Longhi et al.* [1992] divided the Martian mantle, like the terrestrial mantle, into an upper olivine-rich part with STP density 3520 kg m^{-3}, a transition zone composed of silicate-spinel with STP density 3720 kg m^{-3}, and a lower perovskite-rich zone with STP density 4170 kg m^{-3}. Assuming a sulfur content of the core as derived from SNC meteorites (14.5 wt%) and accounting for volume changes upon melting, they calculated a STP density of 6800 kg m^{-3} for the core alloy. The core radius and mass fraction are then $0.5 r_p$ and 22%, and the mean dimensionless moment of inertia factor then turns out to be 0.353.

Since the Martian mantle is relatively iron-rich, the olivine–spinel transition region must be expected to be again subdivided into an upper layer containing olivine and modified spinel in solid solution and a lower layer consisting of spinel and modified spinel in solid solution. *Zharkov et al.* [1991] emphasize that such a transition sequence actually may occur over a depth range of about 500 km. Recently, the high-pressure mineralogy of the transition region and phase relations of iron-rich mantle compositions have been investigated experimentally up to possible Martian core–mantle boundary pressures and temperatures. The sequence of stable phases according to these experiments is α-olivine followed by $(\alpha + \gamma)$-spinel, $(\beta + \gamma)$-spinel, and γ-spinel layers [*Kamaya et al.*, 1993; *Bertka and Fei*, 1996a,b] .

The Martian interior presently experiences tidal distortions produced by annual solar tides and, on shorter timescales, by the Martian satellites Phobos and Deimos. Dissipation of tidal strain energy causes the orbit of Phobos to shrink and that of Deimos to expand. Primarily using long-term ground-based observations of Phobos' orbital longitude, the measured secular rate of acceleration has been estimated to be in the range of 0.00254°to 0.00263°yr^{-1} [*Burns*, 1992]. From the secular acceleration rate, a mean specific dissipation factor Q_p of the Martian interior between 50 and 150 has been estimated for the main tidal period of 0532 hours [*Smith and Born*, 1976]. Using a frequency-dependent absorption band model, *Lognonné and Mosser* [1993] find that these Q_p values are small in comparison with those of the Earth's upper mantle and may indicate either 100 to 150 K lower Martian mantle temperatures and/or smaller deviatoric stresses as a consequence of more sluggish mantle convection. Alternatively, *Zharkov and Gudkova* [1993] argue that the low Q_p values suggest the presence of a liquid metallic core. An entirely liquid core has also been proposed by *Schubert and Spohn* [1990] to explain the apparent lack of a self-generated magnetic field of Mars.

In the present paper, we present new and more complete models of the interior structure based on the SNC chemistry. We specifically consider the effects of compression, thermal expansion and of high-pressure phase transitions in the deep Martian mantle. Two end-

member models are constructed and compared: one (model A) that satisfies the upper limit of $C/M_p r_p^2 = 0.366$ [*Esposito et al.*, 1992] and a second model (model B) that satisfies the chondritic Fe/Si ratio of 1.71. We find that it is not possible to satisfy both constraints simultaneously. The second model being consistent with the geochemical requirement produces $C = 0.357 \times M_p r_p^2$, whereas the first model commensurate with the geophysical constraint gives Fe/Si = 1.35. Profiles of pressure, gravity, temperature, heat flow, density, thermal expansivity, bulk modulus, Grüneisen parameter, pressure derivative of bulk modulus, seismic velocity and parameter, Poisson ratio, kinematic viscosity, and thermal diffusivity are calculated. The mathematical model used for numerical calculations is described in the following section. The third section describes the structural model parameters as derived from the compositional model. The model results are presented in the fourth section and are discussed in the concluding fifth section.

Model

A commonly used approach to modeling the interior structure of a terrestrial planet given its mass, radius, and moment of inertia (see *Wood et al.* [1981] for a review) converts the estimated bulk composition into a mineralogical model and adopts potential temperatures for the mantle layers and the core from thermal history calculations. The potential temperature is the temperature extrapolated adiabatically to the surface pressure. The radial density distribution is then calculated under the assumption of hydrostatic and thermal equilibrium by using an equation of state (EOS) to correct for compression and thermal expansion. The total mass and the moment of inertia are calculated from the model and compared with the data. We extend and modify this procedure by calculating the thermal and mechanical structure of Mars simultaneously. In order to derive such a self-consistent structural model, STP values of the density, the bulk modulus, and the thermal expansivity are calculated from laboratory data for the individual layers of the model.

Governing Equations

Assume a spherically symmetric planet in perfect mechanical and thermal equilibrium. The following set of differential equations for mass m, iron mass m_{Fe}, mean moment of inertia Θ, acceleration of gravity g, pressure p, and heat flow density q can be derived from fundamental principles:

$$\frac{dm}{dr} = 4\pi r^2 \rho_r \tag{1}$$

$$\frac{dm_{\mathrm{Fe}}}{dr} = x_{\mathrm{Fe}} \frac{dm}{dr} \tag{2}$$

$$\frac{d\Theta}{dr} = \frac{8}{3}\pi r^4 \rho_r \tag{3}$$

$$\frac{dg}{dr} = 4\pi \tilde{G} \rho_r - 2\frac{g}{r} - \frac{2}{3}\Omega^2 \tag{4}$$

$$\frac{dp}{dr} = -\rho_r g \tag{5}$$

$$\frac{dq}{dr} = \rho_r \epsilon_r - 2\frac{q}{r} \tag{6}$$

where r is the radial distance from the center of the planet, $\tilde{G}$ is the gravitational constant, Ω the rotation rate, ρ the density, x_{Fe} the concentration of iron per unit mass, and ϵ the specific heat production rate. The subscript r indicates quantities that are local functions of p, T, and composition. In deriving (6) we have neglected heating through viscous dissipation in the convecting mantle because the dimensionless dissipation number $D = \alpha g_p H / c_p$, where α is the thermal expansivity and c_p is the specific heat, is expected to be small owing to the low surface gravity g_p on Mars and the comparatively small thickness $H = r_p - r_{\mathrm{cmb}}$ of the Martian mantle, which is taken as the difference in surface and core radius r_p and r_{cmb}. Viscous dissipation, however, may locally be of importance and may be instrumental in generating melt, as the recent work by *Zhou et al.* [1995] and *Breuer et al.* [1996] has shown.

The base of the rheological lithosphere is defined with the help of the temperature T_{rheo} at which subsolidus creep becomes effective over geologic timescales and which is taken as 0.6 T_m [*Meissner and Vetter*, 1979]. The rheological lithosphere is the upper part of the thicker thermal lithosphere, which additionally comprises the upper cold thermal boundary layer of the convecting mantle and thus represents the thermally conductive outermost layer of the planet [e.g., *Spohn*, 1991]. The boundary temperature at the base of the thermal lithosphere T_{lit} is taken to be 0.85 T_m [*Ranalli*, 1987]. There is an additional core–mantle thermal boundary layer at the bottom of the mantle. The thickness δ of the core–mantle boundary layer is calculated from the local critical Rayleigh number for marginal stability of the layer. The local critical Rayleigh number is [e.g., *Jarvis and Peltier*, 1989]

$$Ra_c = \frac{g\alpha}{\kappa \nu k} q_b \delta^4$$

with the kinematic viscosity ν taken at the geometrically averaged temperature of the boundary layer; q_b is the sum of the basal heat flow density and the heat production rate per unit area $\rho\epsilon\delta$. Within the boundary layers, heat is transported radially by conduction, and the temperature T satisfies

$$\frac{dT}{dr} = -\frac{q}{k_r} \tag{7}$$

where k is the thermal conductivity. Between the boundary layers, energy is primarily transported by convection, and the temperature gradient is assumed to be approximately equal to the adiabatic temperature gradient [e.g., *Stacey*, 1977]

$$\frac{dT}{dr} = T \frac{\gamma_r}{K_{S,r}} \frac{dp}{dr} \tag{8}$$

where $\gamma = \alpha K_S / \rho c_p$ is the thermodynamic Grüneisen parameter and K_S is the adiabatic bulk modulus.

We do not consider layered convection in the Martian mantle. Recent axisymmetric convection calculations [D. Breuer et al., Phase transitions in the Martian mantle: Implications for partially layered convection, submitted to *Earth and Planetary Science Letters*, 1996] indicate that phase transitions may induce some albeit imperfect layering, but the effects of the layering for the temperature profile are entirely speculative at the present time.

The set of basic differential equations (1) – (8) can be separated into two subsets that are coupled through the density ρ. The mechanical properties of the interior are calculated from (1) – (5), while (6) – (8) give the thermal structure of the model. Because ρ depends more strongly on pressure than on temperature, a feature common to planetary bodies, we calculate the density distribution by using an isothermal fourth-order Eulerian finite strain–Murnaghan-Birch equation of state and by applying temperature corrections through a calculation of the thermal pressure as described further below [*Stacey et al.*, 1981].

Phase boundaries, namely, the exothermic olivine–β-spinel and β-spinel–γ-spinel transitions and the endothermic γ-spinel–perovskite transition, are treated as follows: We first simplify the complex olivine–spinel phase diagram by assuming univariant discontinuities between the α-olivine, β-spinel, and γ-spinel layers. This is motivated by recent experiments of *Bertka and Fei* [1996a] revealing that the density increases occur mostly at the upper and lower boundary of the solid solution $(\alpha + \gamma)$-spinel and $(\beta + \gamma)$-spinel region. The radial positions of high-pressure phase transitions in the Martian mantle are obtained from the intersections of the areotherm calculated from (6) through (8) and the corresponding Clausius-Clapeyron curves which are given in polynomial form for magnesium-rich, terrestrial mantle compositions by *Leliwa-Kopystyński and Bakun-Czubarow* [1980] for the olivine–β-spinel transition and by *Chopelas et al.* [1994] for the β-spinel–γ-spinel and γ-spinel–perovskite transitions. As compared to the terrestrial mantle ($Mg\# = 0.9$), where $Mg\# = Mg^{2+}/(Mg^{2+} + Fe^{2+})$, however, the iron-rich Martian mantle composition ($Mg\# = 0.75$) causes a significant reduction of the olivine–β-spinel and β-spinel–γ-spinel transition pressures by about 1.5 and 4 GPa, respectively [*Akaogi et al.*, 1989; *Bertka and Fei*, 1996a], which is taken into account (see Table 1). The convective transport of mantle material across a sharp phase boundary is accompanied by a sudden change Δq in heat flow density due to the release or absorption of latent heat, which is given by

$$\Delta q = \Delta H_L \bar{\rho} u_r \tag{9}$$

where $\bar{\rho}$ is the average density of both low- and high-pressure phases and

$$\Delta H_L = T \left(\frac{dP}{dT}\right)_{\text{clap}} \frac{\Delta\rho}{\rho_1 \rho_2} \tag{10}$$

is the latent heat. The latter is calculated from the slope of the Clausius-Clapeyron curve $(dP/dT)_{\text{clap}}$ and the density difference $\Delta\rho$ between the phases. Since the phase boundary is required to remain fixed on the Clausius-Clapeyron curve, the boundary will be displaced to higher pressures by approximately

$$\Delta p \approx -\frac{H_L}{\bar{c}_p} \left(\frac{dP}{dT}\right)_{\text{clap}} \tag{11}$$

where $\bar{c}_p$ is the average specific heat of both phases. The mean convection speed u_r can be estimated from the Nusselt number

$$Nu = 2 \left(\frac{Ra}{Ra_c}\right)^{1/3} \tag{12}$$

as a measure for the efficiency of convection in comparison to heat conduction to be

$$u = u_0 Nu^2 \tag{13}$$

Here, Ra is the mantle Rayleigh number; Ra_c, taken as 657.5, is the critical Rayleigh number for marginal stability; and u_0 is a convection speed scale given by the ratio κ/H between the mantle thermal diffusivity $\kappa = k/\rho c_p$ and the mantle thickness H.

Boundary Conditions

The set of basic differential equations (1) – (8) can be solved by numerical integration satisfying the boundary conditions introduced below and using the parameter values summarized in Table 1. The central boundary conditions at $r = 0$ are

$$\begin{aligned} m &= 0 \\ m_{\text{Fe}} &= 0 \\ \Theta &= 0 \\ g &= 0 \\ p &= p_c \\ q &= 0 \\ T &= T_c \end{aligned} \tag{14}$$

Since there are three observational constraints on the model, the mass, the radius, and the polar moment of inertia or the global Fe/Si ratio, we can choose three parameters as adjustable, the values of which are iteratively adjusted such that the observational constraints can be satisfied. These parameters are the central pressure p_c, the central temperature T_c, and the pressure at the core-mantle boundary p_{cmb}.

The surface boundary conditions at $r = r_p$ are

$$\begin{aligned} m &= M_p \\ m_{\text{Fe}} &= M_{\text{Fe}} \\ \Theta &= I \\ g &= g_p \\ p &= p_p \\ q &= q_p \\ T &= T_p \end{aligned} \tag{15}$$

The mean moment of inertia I is related to the polar moment C and the hydrostatic value of the gravitational oblateness J_2^h by [*Munk and MacDonald*, 1975]

Table 1. Global Properties of Mars

	Value
Planetocentric constant $\tilde{G}M_p$, $m^3\ s^{-2}$	4.28283×10^{13}
Global mass M_p, kg	6.41850×10^{23}
Mean surface radius r_p, km	3389.92
Dimensionless polar moment of inertia estimate $C/M_p r_p^2$	0.345–0.376
Core-mantle heat flow density estimate $q_{\rm cmb}$, mW m^{-2}	3.02
Perovskite-spinel transition pressure $p_{\rm sp-pv}$, GPa	$p = 22.9$ $- 2.5 \times 10^{-3}(T - 2260)$
β-γ-spinel transition pressure $p_{\beta-\gamma}$, GPa	$p = 22.9$ $+ 5 \times 10^{-3}(T - 2260)$ $- 16.7(1 - Mg\#)$
olivine-β-spinel transition pressure $p_{\rm ol-sp}$, GPa	$p = 7.82$ $+ 4.57 \times 10^{-3}T$ $- 0.7 \times 10^{-6}T^2$ $+ 0.007 \times 10^{-9}T^3$ $- 5.4\ (1 - Mg\#)$
Mean specific dissipation factor estimate Q_p	50–150
Surface pressure p_p, Pa	560
Surface temperature T_p, K	210
Period of rotation $\tau_{\rm rot}$, s	8.86427×10^4
Period of revolution $\tau_{\rm rev}$, s	5.92314×10^7
Period of main Phobos tide $\tau_{\rm tid}$, s	1.992×10^4
Obliquity ψ, deg	25.2

References: *Smith and Born* [1976], *Leliwa-Kopystyński and Bakun-Czubarow* [1980], *Spohn* [1991], *Thomas* [1991], *Kieffer et al.* [1992], *Chopelas et al.* [1994], and *Bertka and Fei* [1996a].

$$\frac{I}{M_p r_p^2} = \frac{C}{M_p r_p^2} - \frac{2}{3} J_2^h \tag{16}$$

While the mass M_p and the mean surface values of gravity g_p, pressure p_p, and temperature T_p are well known from spaceborne and Earth-based observations, the surface heat flow density q_p is still unknown. Therefore the boundary condition for the heat flow density is taken at the core–mantle boundary rather than at the surface. This is convenient because the heat flow in the mantle and in the crust depends on the bulk chemistry, which differs between models A and B. The heatflow from the core into the base of the mantle $q_{\rm cmb}$ strongly depends on the past thermal history of the core. Since a detailed modeling of the thermal history is beyond the scope of this paper, a present-day heat flow density of 3 mW m^{-2} is adopted from the recent thermal history calculations of *Spohn* [1991].

Numerical Solution

A modified predictor–corrector integration scheme using the Adams–PECE (Predictor step; Evaluation of derivatives; Corrector step; Evaluation of derivatives) method [*Shampine and Gordon*, 1975] has been chosen to numerically solve (1) – (8). Furthermore, a shooting method using a multidimensional globally convergent Newton–Raphson iteration [*Press et al.*, 1992] has been employed in order to simultaneously adjust the free parameters of the system, namely, p_c, T_c, $p_{\rm cmb}$, $p_{\rm cr}$, q_p, and the global ratio Fe/Si for model A and the moment of inertia factor $C/M_p r_p^2$ for model B. We let integration proceed from the center outward and, at the same time, from the surface inward. The solutions are required to match at an arbitrarily chosen matching point. We use the olivine–spinel transition as the matching point and iterate until the successful solution requiring continuity of all components is met at the internal fitting point within a prescribed numerical accuracy. For the sake of rapid convergence against the sucessful solution, the initial set of starting parameters is constrained to lie sufficiently close to the final set of parameters.

Structural Model Parameters

The chemical composition of Mars has been inferred from concentrations of incompatible elements observed in SNC meteorites and from general cosmochemical constraints. We adopt this model as a baseline and refer the reader to *Longhi et al.* [1992] for a review. In this model the main oxides MgO, Al_2O_3, SiO_2, CaO, and FeO account for 98 wt% of the composition of the primitive Martian mantle and crust, whereas the elements Fe, Ni, and S account for close to 99.5 wt% of the core mass [*Wänke and Dreibus*, 1988]. We further adopt the assumption that the Martian crust is primarily basaltic in composition and is best represented by the shergottite-type meteorites. The mineralogic composition of the crust layer as given by *Babeyko et al.* [1993] is summarized in Table 2 along with the surface concentrations of radiogenic elements believed to be representative for young volcanic terrain on Mars. From the assumption of additive partial molar volumes of crust, mantle, and core components, it is possible to estimate self-consistently the STP parameter values required for evaluating the corresponding equation of state. Polymorphic phase changes within the Martian mantle can then be attributed to the structure of the SiO_2 component [*Reynolds and Summers*, 1969]. Following that approach, we allow for the high-pressure quartz modification stishovite to be present within a possible perovskite layer and for the low-density quartz modification coesite to represent the olivine layer. To account for the experimentally determined magnitudes of the density increases across the olivine–spinel transitions [e.g., *Bertka and Fei*, 1996b], we simply assume coesite and stishovite components to be mixed in equal proportions by volume within the β-spinel zone and in proportions 1:3 by volume within the γ-spinel zone. The relative abundances of mantle oxides, mantle radiogenic elements, and core components are summarized in Table 2. Note that sulfur in the core $x_{\rm S}$ (14.2 wt%) is assumed to be present as FeS with

$$x_{\rm FeS} = \frac{x_{\rm S}}{0.3647} \tag{17}$$

where 0.3647 is the value of the atomic mass fraction

Table 2. SNC-Derived Bulk Composition of Mars

Component	Primitive Mantle	Shergottite Crust [a]
MgO, wt%	30.20	7.50
Al_2O_3	3.02	10.50
SiO_2	44.40	50.50
CaO	2.45	10.30
FeO	17.90	17.80
H_2O, ppm	35.00	180.00
K, ppm	305.00	2500.00
Th, ppb	56.00	2000.00
U	16.00	550.00
or, wt%	...	0.50
plag	...	34.80
cpx	18.80	25.10
opx	31.50	36.70
ol	49.50	0.30
ga	0.30	...
Core		
Fe (γ-iron), wt%	52.99	...
Ni	7.60	...
FeS (hpp)	39.05	...

References: *Wänke and Dreibus* [1988], *Surkov et al.* [1989], *Wänke* [1991], *Carr and Wänke* [1992], *Longhi et al.* [1992], and *Babeyko et al.* [1993].

[a]Radiogenic element concentrations taken from Viking lander ground truth.

$\mu_S/(\mu_S + \mu_{Fe})$ [*Schubert and Spohn*, 1990]. A least squares fit to the iron melting data obtained by *Boehler* [1986] provides the parameterization of the core liquidus

$$T_m = 1809\,(1 - \alpha x_S)\,(1.0145 + 1.215 \times 10^{-2} p - 1.159 \times 10^{-4} p^2) \quad (18)$$

as polynomial function of pressure in units of GPa, where $\alpha \approx 2$ is a constant factor to account for the depression of the melting temperature in the presence of sulfur ($x_S \ll 1$) [*Stevenson et al.*, 1983].

Equation of State

STP parameter values of density ρ_{ref}, mean atomic mass $\bar{\mu}$, thermal expansivity α_{ref}, isothermal bulk modulus $K_{T,ref}$, and rigidity G_{ref} of an assemblage of n components are calculated from volume-weighted averages using the Voigt-Reuss-Hill method [*Watt et al.*, 1976] according to

$$\rho_{ref} = \left(\sum_{i=1}^{n} \frac{x_i}{\rho_i} \right)^{-1} \quad (19)$$

$$\bar{\mu} = \left(\sum_{i=1}^{n} \frac{x_i}{\mu_i} \right)^{-1} \quad (20)$$

$$\alpha_{ref} = \rho_{ref} \sum_{i=1}^{n} \frac{x_i \alpha_i}{\rho_i} \quad (21)$$

$$K_{T,ref} = \left(\rho_{ref} \sum_{i=1}^{n} \frac{x_i}{\rho_i K_{T,i}} \right)^{-1} \quad (22)$$

$$G_{ref} = \left(\rho_{ref} \sum_{i=1}^{n} \frac{x_i}{\rho_i G_i} \right)^{-1} \quad (23)$$

where x_i is the mass fraction of an individual crust, mantle, or core component with STP density ρ_i, mean atomic mass $\bar{\mu}_i$, thermal expansivity α_i, isothermal bulk modulus $K_{T,i}$, and rigidity G_i as listed in Table 3.

Because temperatures within the interiors of terrestrial planets exceed the Debye temperature [e.g., *Anderson et al.*, 1992], the product

$$\alpha K_T = -\left(\frac{1}{\rho} \frac{\partial \rho}{\partial T} \right)_p \times \left(\rho \frac{\partial p}{\partial \rho} \right)_T = \left(\frac{\partial p}{\partial T} \right)_V \quad (24)$$

of the thermal expansivity α and the isothermal bulk modulus K_T is taken to be constant throughout chemically homogeneous layers. This is the quasi-harmonic approximation that has most recently been defended by *Anderson et al.* [1995].

From the thermodynamic identity [e.g., *Anderson*, 1989]

$$\left(\frac{dM}{dT} \right)_V = \left(\frac{dM}{dT} \right)_p + \alpha K_T \left(\frac{dM}{dp} \right)_T \quad (25)$$

for any thermodynamic function M in combination with Swenson's law [*Anderson et al.*, 1992]

$$\left(\frac{dK_T}{dT} \right)_V = 0 \quad (26)$$

the first temperature derivatives dK_T/dT, $d\alpha/dT$, and dG/dT used in the high-temperature limit for making linear temperature corrections to the equation-of-state parameters can be attributed to well-known physical properties under STP conditions according to

$$\frac{dK_T}{dT} = -\alpha_{ref} K_{T,ref} \left(\frac{dK_T}{dp} \right)_{ref} \quad (27)$$

$$\frac{d\alpha}{dT} = \alpha_{ref}^2 \left(\frac{dK_T}{dp} \right)_{ref} \quad (28)$$

$$\frac{dG}{dT} = -\alpha_{ref} G_{ref} \left(\frac{dK_T}{dp} \right)_{ref} \quad (29)$$

where $(dK_T/dp)_{ref}$ is the first pressure derivative of the isothermal bulk modulus as obtained from Voigt-Reuss-Hill averaging over individual components in the reference state. Furthermore, the first pressure derivative of rigidity is simply taken as [*Poirier and Liebermann*, 1984]

$$\left(\frac{dG}{dp} \right)_{ref} = \frac{G_{ref}}{K_{T,ref}} \left(\frac{dK_T}{dp} \right)_{ref} \quad (30)$$

Using the truncation in Eulerian strain at fourth order,

Table 3. Equation-of-State Parameters for Crust and Mantle and Core Components Under STP Conditions ($p_{\mathrm{ref}} = 10^5$ Pa, $T_{\mathrm{ref}} = 298$ K)

	ρ_{ref}, kg m^{-3}	α_{ref}, 10^{-5} K^{-1}	$K_{T,\mathrm{ref}}$, GPa	$\left(\frac{dK_T}{dp}\right)_{\mathrm{ref}}$,	G_{ref}, GPa	Θ_D, K
			Crust			
or	2570	1.400	57.0	5.00	23.9	546
plag	2640	1.400	92.0	5.00	31.2	546
cpx	3320	2.700	128.0	4.50	75.5	662
opx	3604	2.700	103.4	5.00	65.0	651
ol	3813	2.600	127.7	5.10	66.5	638
			Mantle			
MgO	3587	3.090	160.6	3.87	129.4	936
Al_2O_3	3986	1.570	249.5	4.38	162.0	1042
SiO_2, ol	2911	1.066	111.3	5.80	59.0	675
SiO_2, β-spinel	3465	1.200	146.8	5.40	84.5	863
SiO_2, γ-spinel	3834	1.290	185.5	5.20	118.0	956
SiO_2, pv	4287	1.400	275.9	5.00	232.0	1050
CaO	3340	3.798	114.8	5.82	81.1	670
FeO	5987	3.600	178.2	7.00	44.1	493
			Core			
Fe (γ-iron)	8094	7.700	172.0	4.95	103.2	470
Ni	8910	7.700	172.0	4.95	103.2	450
FeS (hpp)	5330	3.800	125.8	4.83	75.5	470

References: *Robie et al.* [1978], *Ahrens* [1979], *Sumino and Anderson* [1984], *Boehler et al.* [1990], and *Mao et al.* [1990].

we subsequently infer the pressure dependence of the elastic moduli G and K_T and its local pressure derivative dK_T/dp [*Stacey et al.*, 1981; *Bina and Helffrich*, 1992]:

$$K_T = K_{T,0}(1-2f)^{5/2}\left\{1 - f\left(5 - 3\left(\frac{dK_T}{dp}\right)_{\mathrm{ref}}\right) + \frac{f^2}{2}\left[9K_{T,0}K''_{T,0} + \left(3\left(\frac{dK_T}{dp}\right)_{\mathrm{ref}} - 7\right)\left(3\left(\frac{dK_T}{dp}\right)_{\mathrm{ref}} - 5\right)\right]\right\} \quad (31)$$

$$G = G_0(1-2f)^{5/2}\left\{1 - f\left(5 - 3\left(\frac{dG}{dp}\right)_{\mathrm{ref}}\frac{K_{T,0}}{G_0}\right) + \frac{f^2}{2}\left[9G''_0\frac{K^2_{T,0}}{G_0} + 9\left(\frac{dG}{dp}\right)_{\mathrm{ref}}\frac{K_{T,0}}{G_0}\left(\left(\frac{dK_T}{dp}\right)_{\mathrm{ref}} - 4\right) + 35\right]\right\} \quad (32)$$

$$\frac{dK_T}{dp} = \left(\frac{dK_T}{dp}\right)_{\mathrm{ref}} + 3K_{T,0}K''_{T,0}f \quad (33)$$

with

$$f = \frac{1}{2}\left[\left(\frac{\rho}{\rho_0}\right)^{2/3} - 1\right] \quad (34)$$

where the double prime indicates the second derivative with respect to pressure. As reliable measurements of $K''_{T,0}$ and G''_0 are yet unavailable for materials believed to be present in the Martian mantle, we instead may assume

$$G''_0\frac{K^2_{T,0}}{G_0} \approx -\frac{35}{9} \quad (35)$$

and [*Hofmeister*, 1991]

$$K_{T,0}K''_{T,0} \approx -\left(\frac{dK_T}{dp}\right)^2_{\mathrm{ref}} + 7\left(\frac{dK_T}{dp}\right)_{\mathrm{ref}} - \frac{143}{9} \quad (36)$$

To calculate the seismic structure of the Martian interior in terms of the P and S wave velocities,

$$v_p = \sqrt{\frac{K_S + \frac{4}{3}G}{\rho}} \quad (37)$$

and

$$v_s = \sqrt{\frac{G}{\rho}} \quad (38)$$

we finally employ the isothermal–adiabatic transformation

$$\frac{K_S}{K_T} = 1 + \gamma\alpha T \quad (39)$$

between adiabatic bulk modulus K_S and its isothermal counterpart K_T by using Slater's formulation

$$\gamma \approx \frac{1}{2}\frac{dK_T}{dp} - \frac{1}{6} \tag{40}$$

as a valid approximation of the thermal Grüneisen parameter γ [e.g., *Stacey*, 1977].

Additional constitutive equations as described in the following section together with the above equations permit to extrapolate any local physical quantities to higher pressures and temperatures within safe (P,T) limits by simply proceeding from a well-known reference state $(p_{\mathrm{ref}},T_{\mathrm{ref}})$.

Transport Properties

The important heat transport parameters are the thermal conductivity k and the kinematic viscosity ν. The transport of energy within the convective regions of the planet depends on ν through the vigor of the convection, which is a strong function of ν. The thermal conductivity depends on the state variables volume, pressure, and temperature. The total thermal conductivity is the sum of the lattice or phonon conductivity and the radiative or photon conductivity. The lattice thermal conductivity is an anharmonic quantity like the thermal expansivity, and can be related to the above equation-of-state parameters according to

$$k_l = \frac{1}{3}\bar{a}\frac{\bar{v}K_S}{\gamma^2 T} \tag{41}$$

where $\bar{v}$ is mean sound velocity and $\bar{a}$ is mean interatomic distance. If it is assumed that the minimum wavelengths of the vibrational modes are equal to $2\bar{a}$, the mean interatomic distance is approximately given as

$$\bar{a} \approx \pi\frac{\hbar}{k_b}\frac{\bar{v}}{\Theta_D} \tag{42}$$

where $\hbar$ is Planck's constant normalized to 2π and k_b is Boltzmann's constant [*Poirier*, 1991]. Using Debye's approximation, the local value of the Debye temperature $\Theta_D \propto \bar{v}$ can be related to the mean sound velocity by

$$\bar{v} = \left[\frac{1}{3}\left(\frac{2}{v_s^3} + \frac{1}{v_p^3}\right)\right]^{-1/3} \tag{43}$$

where v_s and v_p are the S and P wave velocities, respectively [e.g., *Anderson*, 1989]. The photon conductivity in the deep interior of Mars can be of the same order of magnitude as the lattice conductivity because a significant amount of energy can be carried by thermal photons at sufficiently elevated temperatures. The radiative heat transfer is characterized by the T^3 dependence of the radiative conductivity k_r according to [e.g., *Poirier*, 1991]

$$k_r = \frac{16}{3}\frac{n^2}{\langle\epsilon\rangle}\sigma_B T^3 \tag{44}$$

where σ_B is Stefan-Boltzmann constant, $n \approx 1.7$ is index of refraction, and $\langle\epsilon\rangle$ taken as 2000 m^{-1} is the mean opacity of mantle rock as averaged over the relevant spectral range of radiation.

The parameterization of the mantle viscosity η_{st} to describe the thermally activated stationary creep deformation poses another problem. The viscosity is known to be a strong function of pressure and temperature [*Weertman and Weertman*, 1975]. A viscoelastic stress relaxation timescale τ can be defined in terms of the Gibbs activation energy G^* [*Turcotte and Schubert*, 1982]

$$\tau = 2\frac{\eta_{\mathrm{st}}}{E} = \tau_0 \exp\left(\frac{G^*}{RT}\right) \tag{45}$$

where E is Young's modulus, R is the universal gas constant, and τ_0 is a characteristic atomic oscillation timescale in the 10^{-13} s range depending on the local Debye temperature. The activation parameters are related to each other by [*Sammis et al.*, 1981; *Anderson*, 1989]

$$G^* = K_T\left(\frac{dK}{dp} - 1\right)^{-1} V^* \tag{46}$$

and

$$V^* = \frac{E^* dT_m/dp}{T_m - p\,dT_m/dp} \tag{47}$$

where V^* is the activation volume and $E^* = a^* R T_m$ with dimensionless activation constant $a^* \sim 18$ for metals and $a^* \sim 30$ for silicates as widely used approximations for the activation energy E^* in the high-temperature range. Note, however, that the value of the activation constant must be expected to vary with depth, since a^* is affected by crystal structure as well as by the dominant creep mechanism, e.g., by either diffusion of atoms and dislocations through grains or transport along grain boundaries [*Weertman and Weertman*, 1975]. Furthermore, based on numerical studies of convection with Newtonian or power law rheology, *Christensen* [1989] emphasizes the side effect of overestimating the influence of pressure and temperature on rheology when neglecting the stress dependence. Consequently, the effective viscosity would decrease under high stresses and increase under low stresses, resulting in a much weaker increase in viscosity with depth [*Christensen*, 1989]. Upon using the Lindemann law,

$$\frac{dT_m}{dp} = 2T_m\frac{\gamma - 1/3}{K_T} \tag{48}$$

together with the definition for γ as given in (40), we may arrive at

$$\eta_{\mathrm{st}} = \frac{1}{2}E\tau_0 \exp\left(a^*\frac{T_m}{T\left(1 - \frac{p}{T_m}\frac{dT_m}{dp}\right)}\right) \tag{49}$$

which gives us a way to estimate the radial distribution of stationary mantle viscosity. To account for the reduction of mantle viscosity in the presence of volatile components such as H_2O and CO_2, (49) is finally replaced with the expression

$$\eta_{\rm st} = \frac{1}{2} E \tau_0 \exp\left(a^* \frac{T_m + \frac{\theta}{a^*} x_{\rm vol}}{T} \right) \quad (50)$$

where $x_{\rm vol}$ is the total weight fraction of volatiles as adopted from the SNC chemistry (see Table 2) and $p/T_m dT_m/dp \ll 1$ is assumed. Analogous to terrestrial mantle lherzolithes believed to represent depleted mantle rock, the parameter θ is taken as -3.5×10^6 K throughout the Martian mantle. Melting temperatures in the mantle are calculated as a function of pressure in units of GPa by using the relation

$$p = \frac{T_m - 1373}{136} + 4.968 \times 10^{-4} \exp(1.2 \times 10^{-2}(T_m - 1373)) \quad (51)$$

which has been established from various melting experiments conducted over a wide range of confining pressures [*McKenzie and Bickle*, 1988].

We tentatively constrain the radial distribution of effective viscosity by simply adjusting the value of a^* until the mean specific dissipation function Q_p of the Martian interior as inferred from Phobos' secular acceleration can be matched. Considering only steady state mechanisms of attenuation in the limit of low stressing frequency, the Maxwell rheological model can be best employed to relate viscosity to a material dissipation factor Q_μ given by

$$Q_\mu = \frac{\eta_{\rm st}}{G} \omega \quad (52)$$

where ω is stressing frequency to be identified with the tidal frequency of the main Phobos tide. It is, however, a still unresolved issue as to whether the Maxwell rheological model is of any value regarding the tidal frequency band Mars is subject to owing to the Phobos tide. In order to account for both transient and stationary creep mechanisms, we therefore decide to replace the common Maxwell rheological model with the more general linear Burgers rheology by substituting (52) for

$$Q_\mu = \frac{\eta_{\rm st}}{G_\infty} \omega \frac{1 + \frac{G_\infty}{G_{\rm tr}} + \left(\frac{\eta_{\rm tr}}{G_{\rm tr}} \omega \right)^2}{1 + \left(1 + \frac{\eta_{\rm st}}{\eta_{\rm tr}} \right) \left(\frac{\eta_{\rm tr}}{G_{\rm tr}} \omega \right)^2} \quad (53)$$

where $\eta_{\rm tr}$ is transient viscosity in contrast to $\eta_{\rm st}$ as the stationary viscosity mentioned above. Likewise, $G_{\rm tr}$ is transient rigidity and G_∞ denotes unrelaxed, i.e. elastic shear modulus. As a rough guide for the Martian mantle, we adopt the ratios of transient to stationary parameters as determined by *Smith and Carpenter* [1987] for typical materials likely being present in the Earth's mantle. The given rigidity ratio $G_{\rm tr}/G_\infty$ approximately centered at 0.1 seems to depend strongly on the ambient homologous temperature field as well as on hydrous conditions. The viscosity ratio is confined to the range 0.5 (olivine) $< \eta_{\rm tr}/\eta_{\rm st} <$ 0.75 (garnet).

Heat Sources

Since the distribution of heat sources within a planetary body cannot be addressed with real confidence owing to the complex differentiation history, we, for simplicity, employ an exponentially decreasing distribution of crustal radiogenic elements with depth according to [*Toksöz et al.*, 1978]

$$\epsilon^*_{\rm cr} = \epsilon_0 \exp\left(-\frac{r_p - r}{h_e} \right) \quad (54)$$

where the skin depth h_e is the depth for crustal heat production to decrease by a factor of e and ϵ_0 is the specific heat production rate upon radioactive decay at the surface as obtained from Mars 5 and Phobos 2 gamma ray orbital data and Viking 1 and 2 soil analysis [*Surkov et al.*, 1989]. The latter can be obtained from

$$\epsilon_0 = c_0^{\rm U} \left(\epsilon^{\rm U} + \frac{c_0^{\rm Th}}{c_0^{\rm U}} \epsilon^{\rm Th} + \frac{c_0^{\rm K}}{c_0^{\rm U}} \epsilon^{\rm K} \right) \quad (55)$$

where $c_0^{\rm U}$, $c_0^{\rm Th}$, $c_0^{\rm K}$ are surface concentrations of uranium, thorium, and potassium as given in Table 2 for SNC meteorites and $\epsilon^{\rm U} = 9.71 \times 10^{-5}$ W kg^{-1}, $\epsilon^{\rm Th} = 2.69 \times 10^{-5}$ W kg^{-1}, $\epsilon^{\rm K} = 3.58 \times 10^{-9}$ W kg^{-1} are corresponding present-day rates of heat release per unit mass [*Turcotte and Schubert*, 1982]. If we assume that the radiogenic heat production rate is continuous across the crust–mantle boundary at $r_{\rm cr}$, then h_e can be related to the actual crustal thickness $d_{\rm cr} = r_p - r_{\rm cr}$ according to

$$h_e = \frac{d_{\rm cr}}{\ln(\epsilon_0/\epsilon^*_m)} \quad (56)$$

where ϵ^*_m is the present specific heat production of the depleted mantle and can be linked to the potential specific heat production of the undifferentiated, primitive mantle/crust system $\epsilon_{\rm SNC}$ as obtained from geochemical data for the SNC meteorites (see Table 2) via a mantle depletion factor ξ_m. Based on mass balance between crust and mantle reservoirs, this quantity can be written as

$$\xi_m = 1 - \frac{\epsilon^*_m}{\epsilon_{\rm SNC}} = 1 - \frac{\frac{\bar\rho}{\rho_{\rm cr}} (r_p^3 - r_{\rm cmb}^3) - \frac{\epsilon_0}{\epsilon_{\rm SNC}} (h_e r_p^2 - 2 r_p h_e^2 + 2 h_e^3)}{(r_{\rm cr}^3 - r_{\rm cmb}^3) \frac{\rho_m}{\rho_{\rm cr}} - (h_e r_{\rm cr}^2 - 2 r_{\rm cr} h_e^2 + 2 h_e^3)} \quad (57)$$

where $\rho_{\rm cr}$ is the average crust density, ρ_m is the average mantle density, and $\bar\rho$ is the mean density of both reservoirs. Note that $\xi_m = 1$ corresponds to an entirely depleted mantle devoid of radioactives and $\xi_m = 0$ represents the primitive, fertile mantle source. Equations (56) and (57) must be solved iteratively in order to estimate h_e for the Martian crust.

Secular cooling of the interior provides another significant contribution to the planet's present surface heat flow. This can be modeled as a contribution to the specific heat production rate, which is then

$$\epsilon = \epsilon^*_{rn} - c_p \dot{T}_{\rm pot} \quad (58)$$

where $\dot{T}_{\rm pot}$ is the time rate of change of the potential mantle temperature. Most recent thermal evolution calculations that account for the differentiation of the Martian interior by *Breuer et al.* [1993] suggest that $\dot{T}_{\rm pot}$ averaged over the last 500 Ma is between 1.0×10^{-15} K s^{-1} and 1.5×10^{-15} K s^{-1}. For the present study, we adopt an average value of 1.25×10^{-15} K s^{-1}.

In the following, we examine two end-member type models of the internal structure of Mars using identical sets of STP parameter values as derived from the specific SNC chemistry and summarized in Table 4. The most important feature of the first model A is that it meets the geophysical constraint regarding the most probable maximum value $C/M_p r_p^2 = 0.366$ of the dimensionless moment of inertia factor for Mars, whereas the second Model B, in turn, matches the global Fe/Si ratio of 1.71 in accordance with the geochemical requirement of a chondritic bulk composition of the Martian interior.

Results

The results of our modeling are shown in Figures 2 through 10 and are summarized for model A in Table 5 and for model B in Table 6. The global structures of the two models are similar with a crust, an upper and a lower mantle separated by the olivine to spinel transition, and a core. The lower mantle is further subdivided into β-spinel and γ-spinel layers, but a perovskite layer is not found. The core is homogeneous and entirely liquid, thereby lacking a solid inner core. A comparison of the global structure of the two models is presented in Figure 1. The models differ significantly in the thicknesses of the crusts and the radii of the cores. For a simultanous fit of the central and surface boundary conditions given in (14) and (15), model A, constrained mostly by the moment of inertia factor, requires a core of 1468-km radius and a crust of 110-km thickness, whereas model B produces a core with a radius of 1667 km and a 250-km-thick crust. There are less substantial differences in the locations of the olivine–β-spinel transition and the β-spinel to γ-spinel phase boundary and in the thicknesses of the rheological lithosphere. The thermal lithosphere thicknesses differ by about 100 km.

Density and Mechanical Stratification

The density as a function of the radial distance from the planet's center is shown in Figure 2. The density increases almost linearly with depth in the mantle and crust layers and by 600 kg m^{-3} at the crust–mantle boundary and by 250 kg m^{-3} at the olivine–β-spinel phase boundary. The olivine–β-spinel transition is located at a relative radius equal to 0.7 corresponding to a depth of about 1000 km; the β-spinel to γ-spinel transformation should occur close to relative radius 0.6, approximately 300 km (model B) and 550 km (model A) above the core-mantle boundary. Note that the two models differ little in crust and mantle densities despite significant differences in crust thicknesses and core radii. The most significant density increase by about 3000 kg m^{-3} occurs at the core-mantle boundary. In the core, density increases by about 5% with depth,

Table 4. STP Parameter Values Used for Modeling the Interior Structure of Mars

	Fe-FeS Core	Perovskite Zone	γ-Spinel Zone	β-Spinel Zone	Olivine Zone	Crust [a] Layer
$\rho_{\rm ref}$, kg m^{-3}	6772	4224	4014	3822	3493	2799
$\alpha_{\rm ref}$, $10^{-5} \times$ K^{-1}	5.765	2.383	2.282	2.190	2.033	2.142
$K_{T,\rm ref}$, GPa	145.5	200.1	173.6	155.1	130.7	102.3
$G_{\rm ref}$, GPa	87.3	120.3	99.3	85.8	69.3	45.3
$\left(\frac{dK_T}{dp}\right)_{\rm ref}$	4.892	4.777	4.875	4.981	5.209	4.874
$\left(\frac{dG}{dp}\right)_{\rm ref}$	2.935	2.872	2.788	2.754	2.761	2.158
$\left(\frac{d\alpha}{dT}\right)_{\rm ref}$, $10^{-8} \times$ K^{-2}	1.626	0.271	0.254	0.239	0.215	0.224
$\left(\frac{dK_T}{dT}\right)_{\rm ref}$, $10^{8} \times$ Pa K^{-1}	−0.410	−0.228	−0.193	−0.169	−0.138	−0.107
$\left(\frac{dG}{dT}\right)_{\rm ref}$, $10^{8} \times$ Pa K^{-1}	−0.246	−0.137	−0.110	−0.094	−0.073	−0.047
ϵ_0, $10^{-12} \times$ W kg^{-1}	—	4.152	4.152	4.152	4.152	116.2
$\dot{T}_{\rm pot}$, $10^{-15} \times$ K s^{-1}	—	−1.25	−1.25	−1.25	−1.25	−1.25
$G_{\rm tr}/G_\infty$	—	0.1	0.1	0.1	0.1	0.1
$\eta_{\rm tr}/\eta_{\rm st}$	—	0.6	0.6	0.6	0.6	0.6
Θ_D, K	469	894	863	825	727	606
$\bar{\mu}$, $10^{-3} \times$ kg mol^{-1}	50.85	22.09	22.09	22.09	22.09	21.39

[a] The crustal density reference under standard conditions is calculated according to the relation $\rho_{\rm ref} = (0.75/\rho_{\rm liq} + 0.25/\rho_{\rm sol})^{-1}$ where $\rho_{\rm liq} = 2706$ kg m^{-3} is basaltic melt density and $\rho_{\rm sol} = 3122$ kg m^{-3} is solid basalt density, respectively, in accordance with the specific shergottite chemistry and mineralogy.

Table 5. Interior Boundary Values of Mars (Model A)

	Radius, km	Pressure, GPa	Temperature, K	Heat Flow, mW m^{-2}	Mass Fraction	Gravity, m s^{-2}	Iron Mass Fraction
Central Sphere	2	39.03	1950	0.00	0.0000	0.005	0.0000
Core-Mantle Boundary	1468	23.62	1771	3.02	0.1463	2.905	0.1139
Lower Thermal Boundary Layer	1503	23.19	1760	3.48	0.1528	2.895	0.1148
β-Spinel–γ-Spinel Transition	2033	16.56	1674	9.73	0.2923	3.026	0.1350
α-Olivine–β-Spinel Transition	2360	12.47	1612	12.51	0.4157	3.200	0.1530
Thermal Lithosphere	2908	5.87	1483	14.67	0.6858	3.475	0.1921
Rheological Lithosphere	3055	4.05	997	15.25	0.7762	3.564	0.2052
Crust-Mantle Boundary	3280	1.15	411	16.14	0.9327	3.713	0.2278
Physical Surface	3390	0.00	210	25.01	1.0000	3.727	0.2375

and the two models differ in core density by less than 100 kg m^{-3}.

The cumulative radial distribution of mass throughout the Martian interior is shown in Figure 3 for models A and B together with the corresponding iron mass distribution. Almost half of the bulk iron by mass is provided by the core which comprises about 15% of the planet's mass for model A and 21% for model B.

In Figure 4, profiles of the thermal expansivity are shown along with profiles of the isothermal bulk modulus. There is little difference between the two models in the variation of these quantities in the individual layers. Major discontinuities are found at the core-mantle boundary and at the two olivine–spinel transitions. The isothermal bulk modulus increases by about a factor of 2 through the mantle and by about a factor of 1.4 through the core, and the thermal expansivity decreases by about the same factors. The local pressure derivative of the isothermal bulk modulus dK_T/dp is plotted together with the Grüneisen parameter γ calculated from (40) in Figure 5. Both quantities decrease monotonically with depth. There are small jumps at the crust, olivine–spinel, and core–mantle boundaries.

The variations with radial distance from the planet's center of the hydrostatic pressure and the gravitational acceleration are shown in Figure 6. The pressure increases linearly with depth throughout the crust and mantle and parabolically in the core. Pressure at

Table 6. Interior Boundary Values of Mars (Model B)

	Radius, km	Pressure, GPa	Tempera-, ture, K	Heat Flow, mW m^{-2}	Mass Fraction	Gravity, m s^{-2}	Iron Mass Fraction
Central Sphere	2	41.13	2164	0.00	0.0000	0.005	0.0000
Core-Mantle Boundary	1667	21.75	1917	3.02	0.2109	3.250	0.1641
Lower Thermal Boundary Layer	1700	21.28	1906	3.36	0.2188	3.241	0.1652
β-Spinel–γ-Spinel Transition	1974	17.52	1853	6.70	0.2958	3.249	0.1764
α-Olivine–β-Spinel Transition	2332	12.79	1775	9.50	0.4252	3.356	0.1953
Thermal Lithosphere	2783	7.19	1657	10.95	0.6350	3.515	0.2256
Rheological Lithosphere	3016	4.22	1083	11.68	0.7717	3.635	0.2454
Crust-Mantle Boundary	3138	2.64	780	12.07	0.8518	3.705	0.2570
Physical Surface	3390	0.00	210	31.18	1.0000	3.727	0.2784

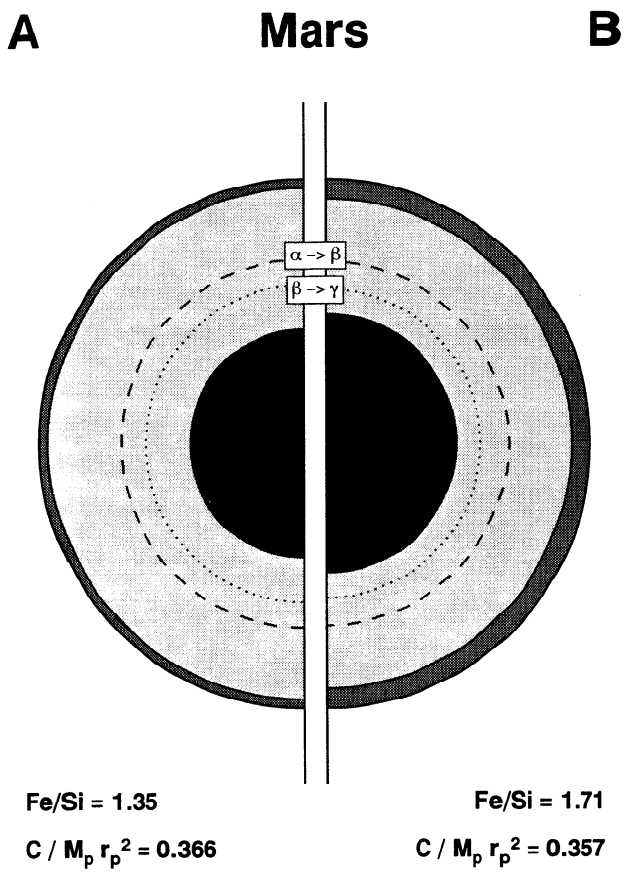

Figure 1. Comparison of the internal structure of Mars for both models A and B. The global structures of the two models are similar, with a basaltic crust, an upper and a lower mantle separated by the α-olivine to β-spinel transition, and a metallic core. The lower mantle is further subdivided into β-spinel and γ-spinel layers. The models differ significantly in the thicknesses of the crusts and the radii of the liquid cores. Fe/Si and $C/M_p r_p^2$ denote the calculated global iron to silicate ratio and the dimensionless polar moment of inertia factor, respectively.

the α−olivine–β-spinel transition and at the β-spinel–γ-spinel transition is found to be close to 13 and 18 GPa, respectively. There are small but significant differences in the pressure in the core between the two models, mainly caused by differences in the core masses. The central pressure is about 39 GPa for model A and 41 GPa for model B. The gravitational acceleration increases linearly with radius throughout the core to values of about 3 m s^{-2} (model A) and 3.3 m s^{-2} (model B) at the core-mantle boundary and approximately parabolically through the mantle.

Thermal Structure

In Figure 7, the present-day areotherms for both models are shown together with the radial distribution of mantle heat flow density. The temperature increase across the crust and thermal lithosphere, where heat is transferred conductively, is found to be about 1300 K (model A) and 1400 K (model B). The subsequent adia-

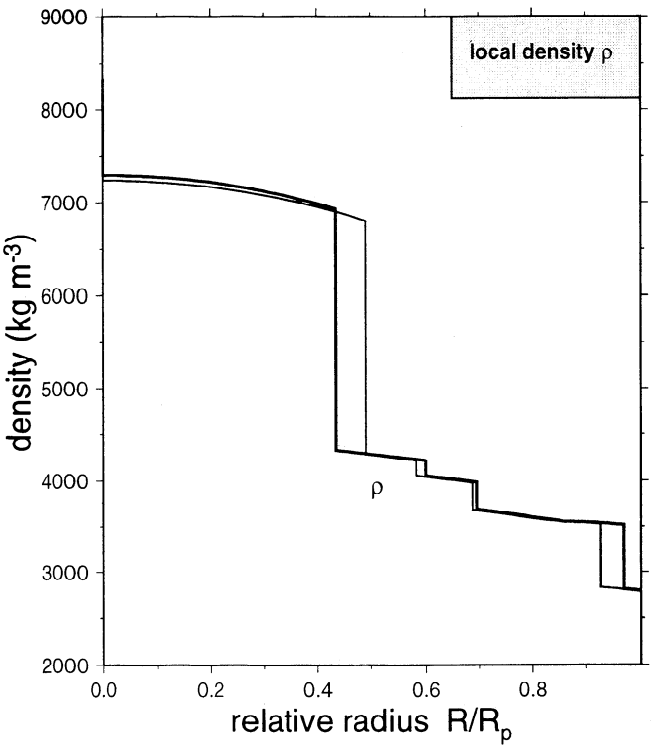

Figure 2. Radial distribution of density for model A (heavy curve) and model B (light curve).

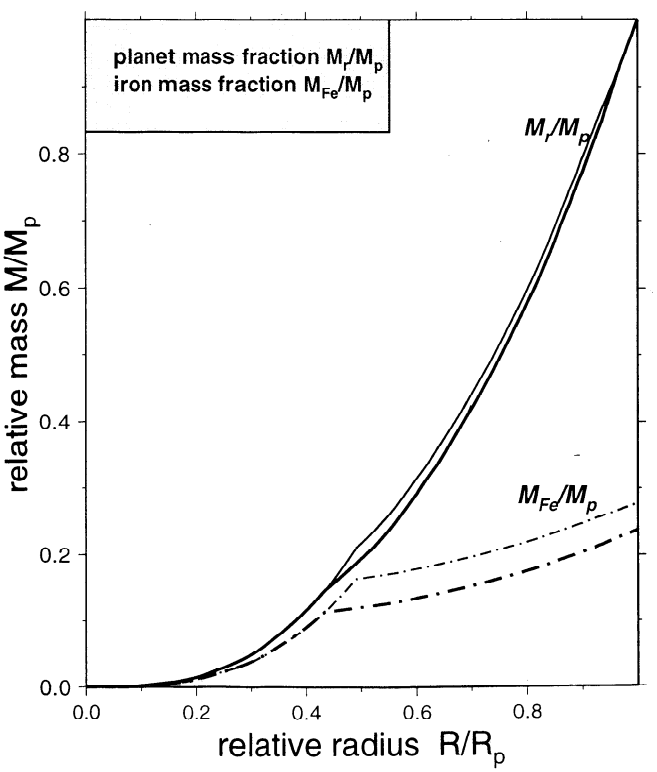

Figure 3. Radial distribution of cummulative planet mass fraction and cummulative iron mass fraction for model A (heavy curve) and model B (light curve).

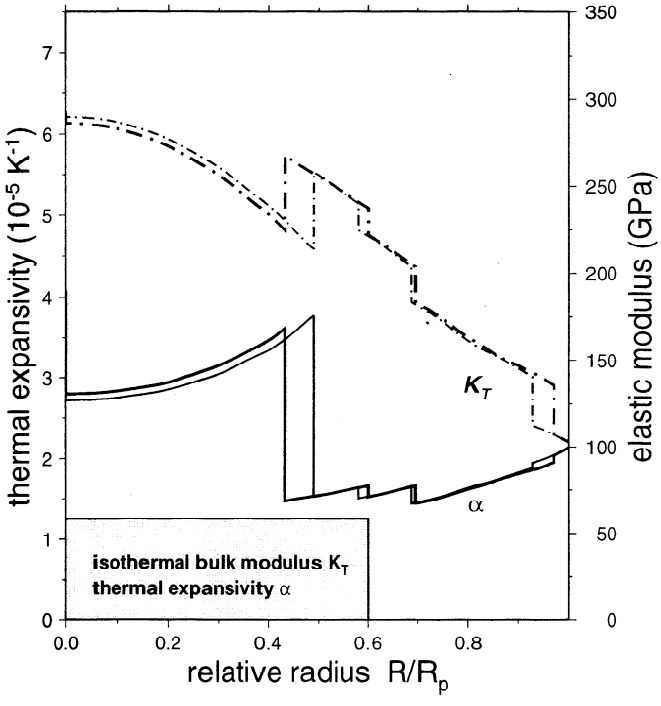

Figure 4. Radial distribution of thermal expansivity and isothermal bulk modulus for model A (heavy curve) and model B (light curve).

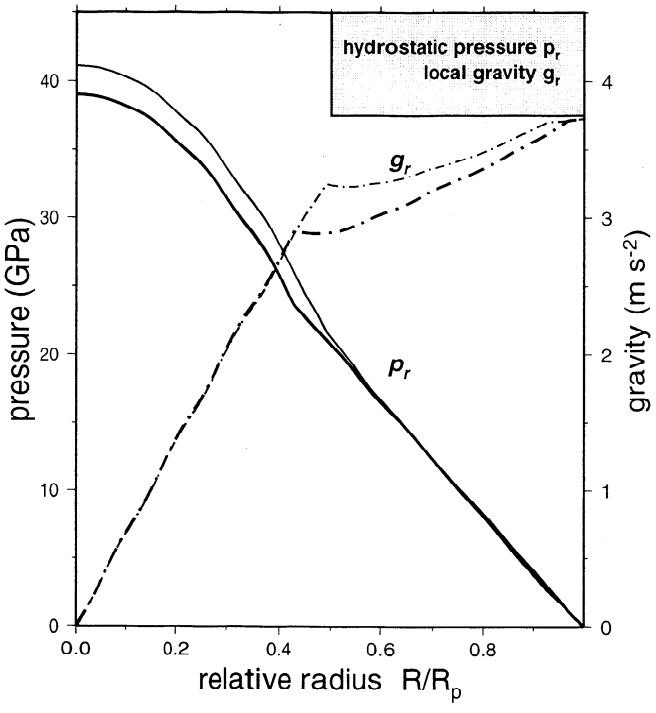

Figure 6. Radial distribution of hydrostatic pressure and gravitational acceleration for model A (heavy curve) and model B (light curve).

batic temperature rise across the convecting upper mantle up to the olivine–β-spinel transition is about 150 K. In the lower mantle the adiabatic temperature increase is about 100 K. The temperature at the core-mantle boundary is found to be between 1750 K for model A and 1900 K for model B. The adiabatic temperature distribution throughout the core turns out to be fairly similar for both models, resulting in central temperatures close to 1950 K (model A) and 2150 K (model B), respectively.

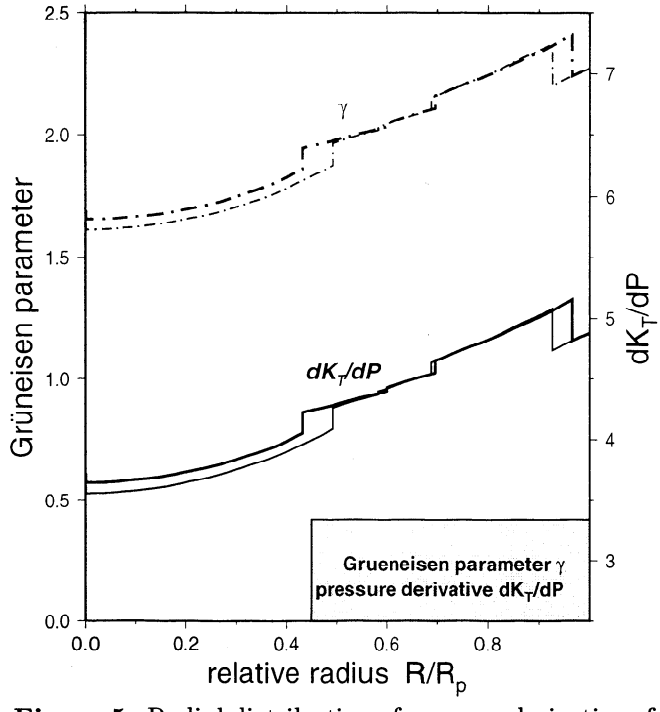

Figure 5. Radial distribution of pressure derivative of isothermal bulk modulus and Grüneisen parameter for model A (heavy curve) and model B (light curve).

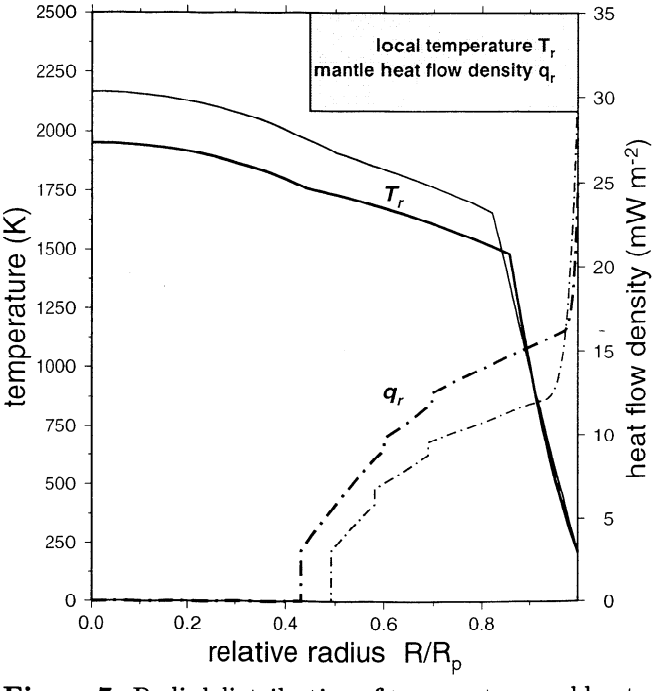

Figure 7. Radial distribution of temperature and heat-flow density for model A (heavy curve) and model B (light curve).

Because model B requires a crust layer of 250 km thickness, as compared with 110 km for model A, the mantle in model B is about 3 times more depleted in radioactive elements than the model A mantle. As a consequence, the heat flow density increases much more rapidly with radius in model A. The heat flow from the core into the mantle is taken to be 3 mW m^{-2} in accordance with results of thermal history calculations by *Spohn* [1991] and by *Breuer et al.* [1993]. There are small jumps in heat flow density at relative radii 0.6 and 0.7 due to the release of latent heat at the olivine–spinel transitions. In the crust, the heat flow density increases rapidly as a consequence of the crust being enriched in radiogenic heat sources with respect to the mantle to surface values of 25 mW m^{-2} for model A and 30 mW m^{-2} for model B.

Seismic and Anelastic Structure

Figure 8 shows profiles of the seismic velocities v_p and v_s. The velocities increase linearly in the crust and mantle layers and parabolically in the core, and there is no low velocity zone in the mantle. The rate of increase with depth of the P and S wave velocities is considerably smaller than in the Earth because of the lower rate of increase of pressure with depth caused by the smaller mass of the planet. The P wave velocity in the crust is about 7.7 km s^{-1} and the S wave velocity is 4 km s^{-1}. In the upper mantle, v_p increases from 8.3 to 9.4 km s^{-1}, while v_s increases from 4.6 to 5.2 km s^{-1}. There are significant velocity increases at the olivine–spinel phase transitions to values of 10 and 5.5 km s^{-1} for v_p and v_s, respectively. As was discussed by

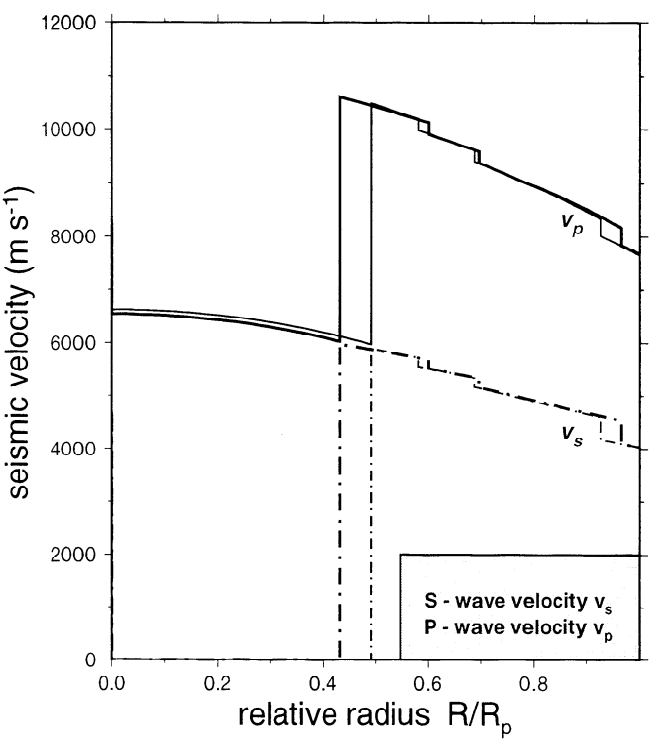

Figure 8. Radial distribution of seismic velocities for model A (heavy curve) and model B (light curve).

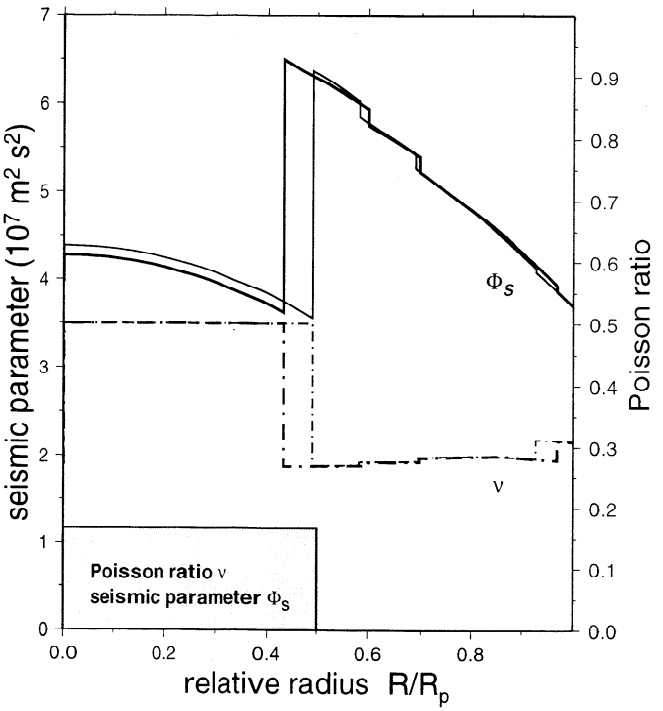

Figure 9. Radial distribution of seismic parameter and Poisson ratio for model A (heavy curve) and model B (light curve).

Okal and Anderson [1978], the discontinuous changes in seismic velocity at the crust–mantle boundary and at the olivine–spinel transitions will result in a triplication of the traveltime curves of seismic phases whose source distance is indicative of the exact radial location of the discontinuity. The P wave velocity in the core is significantly smaller and increases from 6.0 km s^{-1} at the core–mantle boundary to 6.5 km s^{-1} at the center. Since in both models the core is found to be entirely liquid, the propagation of transversal seismic waves is prevented.

Figure 9 gives the radial profile of the seismic parameter

$$\Phi_S = \frac{K_s}{\rho} = v_p^2 - \frac{4}{3}v_s^2 \tag{59}$$

together with Poisson's ratio

$$\nu = \frac{1}{2}\frac{\left(\frac{v_p}{v_s}\right)^2 - 2}{\left(\frac{v_p}{v_s}\right)^2 - 1} \tag{60}$$

as a function of relative radius. While Poisson's ratio varies between 0.25 and 0.3 in the crust and mantle, indicative of the high FeO content, the seismic parameter increases significantly with depth. Note that the discontinuity in Φ_S is small at the crust–mantle boundary but more significant at the olivine–spinel transitions. In both models, a Poisson's ratio of 0.5 indicates the molten state of the core.

To reconcile Mars' global Q_p with an average value of 100 as derived from observational evidence for Phobos'

secular acceleration, values for the dimensionless activation parameter of $a^* = 33.5$ (model A) and $a^* = 36.5$ (model B) are required. The corresponding profiles of the tidally effective viscosity for both models are shown in Figure 10 along with the radial distribution of the thermal diffusivity. The viscosity decreases strongly throughout the lithosphere to a value of 10^{14} m^{-2} s^{-1} as a consequence of the steep conductive temperature gradient. Throughout the adiabatic mantle, the viscosity decreases with depth by roughly 1 order of magnitude, since the strong temperature dependence of viscosity overcompensates the influence of pressure on rheology. The thermal diffusivity is found to decrease considerably with depth through the thermal lithosphere and increases weakly across the adiabatic mantle with minor jumps at the olivine–spinel transitions. It should be emphasized that the tidally effective viscosity in the Martian mantle is several orders of magnitude smaller than the viscosity of the Earth's upper mantle and the viscosity estimated for Mars from thermal evolution calculations [e.g., *Schubert and Spohn*, 1990] because of the low tidal Q_p of Mars. The relation between the tidally effective viscosity and the viscosity of mantle flow is not clear-cut. It is possible, however, that both viscosity profiles would vary in a similar manner with depth. Since the Martian lithosphere is considerably thick, tidal dissipation is expected to be locally enhanced deep within the Martian mantle. As the core is found to be entirely liquid, dissipation in the core will contribute only negligibly small amounts to the internal dissipation of tidal strain energy.

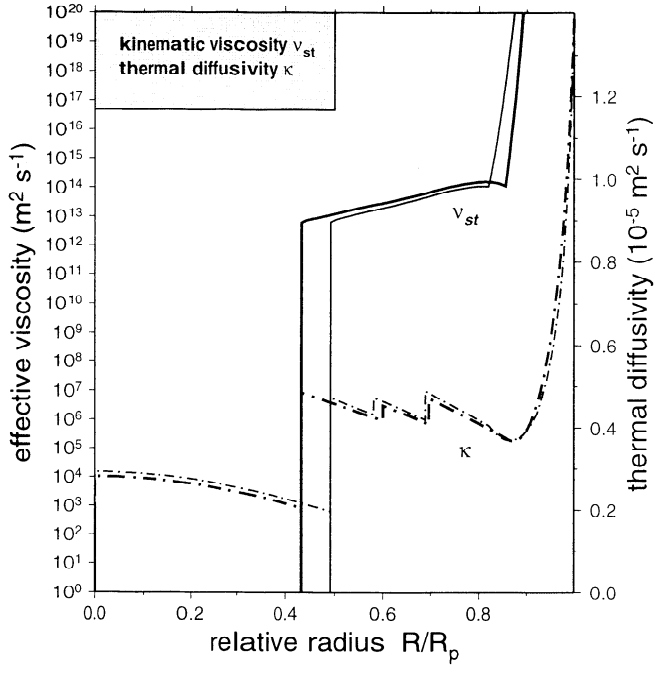

Figure 10. Radial distribution of effective viscosity and thermal diffusivity for model A (heavy curve) and model B (light curve).

Discussion

We have considered two end–member models of Mars' present interior structure optimized either to satisfy the geochemical (model B) requirement of a composition consistent with that of the SNC meteorites or the geophysical requirement of a polar moment of inertia factor with a likely maximum value of 0.366 (model A). The model calculations by means of a numerical equilibrium model that is capable of simultaneously giving the mechanical and thermal structure of the planet, indicate a metallic core size of a little less than one half of the planetary radius surrounded by a silicate mantle region modestly depleted in its initial heat source inventory and subdivided in a lower spinel zone and a less dense upper olivine zone the latter of which overlain by a 100- to 250-km-thick basaltic crust. The considerable upward concentration of radioactives in the crust layer results in a heat flow density of approximately 30 mW m^{-2} at the surface of Mars. The calculated central pressure is about 40 GPa, and the central temperature is found to be about 2000 to 2200 K.

The accuracy of the present results assuming that Fe/Si and $C/M_p r_p^2$ were known exactly is basically limited by uncertainties in the nature of internal chemical, mechanical, and thermal boundaries between consecutive layers, particularly within the mantle, which supposedly cause sharp transitions in physical properties across each boundary. A further source of principal uncertainty lies with the parameterization of the constitutive equations. For instance, we have used the Murnaghan–Birch equation of state for both the mantle and the core. While the applicability of the latter EOS is widely accepted for the mantle, its validity under thermodynamic conditions presumably prevailing in the Fe-FeS core of Mars remains still unwarranted by experimental evidence and is debatable with respect to the actual size and state of the Martian core.

Global Properties

In Figure 11 we compare relative core sizes and dimensionless moment of inertia factors for both models A and B with results of previous work. *Wänke and Dreibus* [1988] as well as *Schubert and Spohn* [1990] calculated two–layered structural models consisting of metallic cores overlain by silicate mantles and ignored the influences of compression, thermal expansion, and the possible existence of high-pressure phase transitions in the mantle. As becomes obvious from an inspection of Figure 11a, these models overestimate the core size. Models that use an equation-of-state such as those of *Ohtani and Kamaya* [1992], *Longhi et al.* [1992], and the present models typically obtain smaller cores. Figure 11b illustrates the fact that a better knowledge of the hydrostatic value of Mars' moment of inertia factor is needed because on grounds of theoretical predictions alone there is too broad a range of possible estimates, imposing no firm constraint on the interior structure of the planet.

The differences in core size between model A and model B result in differences between the periods of several fundamental eigenmodes of free oscillation as listed

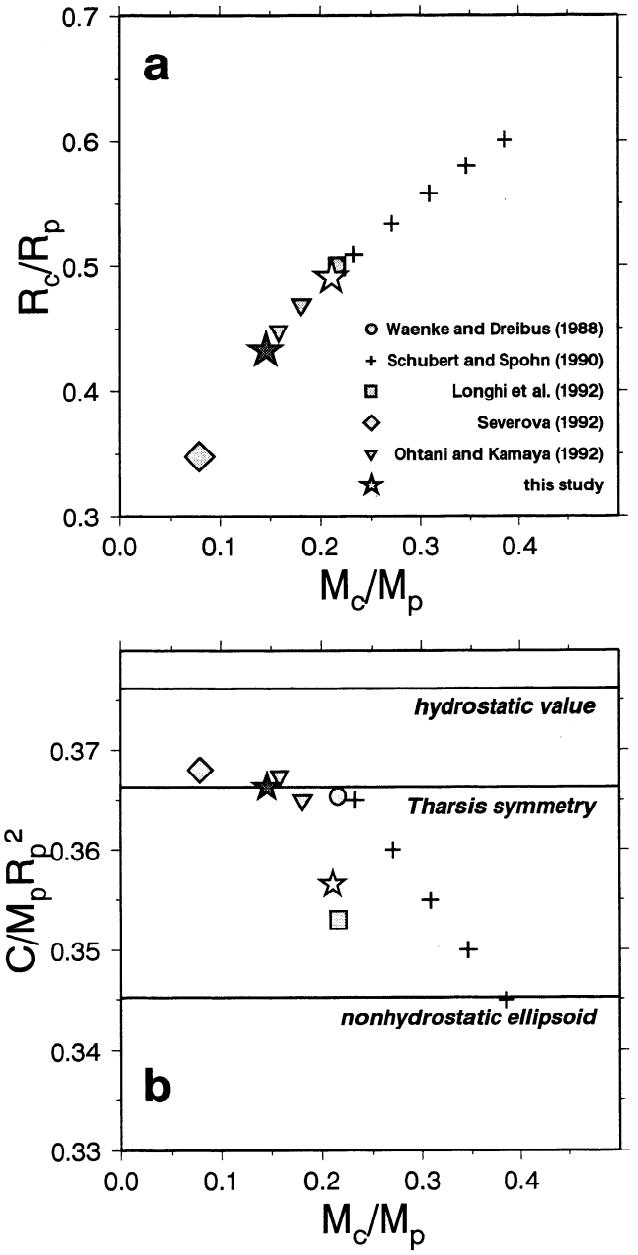

Figure 11. Comparison of relative core sizes and dimensionless moment of inertia factors for several models of Mars' interior structure constrained by the SNC chemistry. Note that the solid star denotes model A, while the open star indicates model B of this study.

in Table 7, where eigenperiods of spheroidal modes ${}_0S_n$ and toroidal modes ${}_0T_n$ of harmonic degree $n \leq 10$ are listed. Note that the modes have been calculated neglecting anelastic properties of the Martian mantle as well as period–splitting of modes through rotational forcing. Since the core is entirely liquid, it is mechanically decoupled from the overlying mantle which results in longer oscillation periods in comparison with models with solid cores [e.g., *Okal and Anderson*, 1978]. Complex Love numbers h_n, k_n, and l_n are listed in Tables 8 and 9 for the periods of tides raised by Phobos $\tau_n = 1104\,\text{hours}/n$. Here it is also assumed that the mantle and crust are elastic and that the core is fluid. The eigenperiods as well as the real and imaginary parts of the complex Love numbers are found to decrease with increasing harmonic degree. This is well in accord with the conventional wisdom that higher modes probe the upper mantle region and lower modes the lower mantle region of a planetary body. Our results confirm the notion of *Gudkova et al.* [1993] that harmonics lower than 5 to 7 would be the most useful to constrain the size and physical state of the Martian core during future Mars lander missions.

In the remainder of this subsection we shall indicate implications for the hydrostatic equilibrium figure of the Martian gravity field and integral properties of the crust and mantle of Mars. In Table 10, we have summarized values of global parameters for both models A and B. Model A, optimized to fit $C/M_pr_p^2 = 0.366$, produces a Fe/Si ratio that is significantly smaller than the chondritic value of 1.71. Model B, optimized to fit the chondritic Fe/Si ratio, requires a larger core size and gives a dimensionless polar moment of inertia factor that is well within the range of reasonable values. On the basis of these differences, model B may be considered preferable over model A because the former satisfies the geochemical constraints in terms of the bulk chondritic Fe/Si ratio while still producing a dimensionless polar moment of inertia factor that is in between the two limits on reasonable values.

As expected for a differentiated planet such as Mars, the resultant values of 1.2 (model A) and 1.1 (model B) for the secular Love number

$$k_2^f = 3\frac{J_2^h}{m} \tag{61}$$

with m the equatorial ratio of gravitational to centrifugal acceleration indicate the considerable concentration of mass toward the center for both models. Table 10 lists the corresponding geometric and dynamic flattenings, $(a-c)/a$ and $(C-A)/C$, respectively, along with the gravity flattening $(g_a - g_c)/g_a$ and the hydrostatic gravitational oblatenesses J_2^h, J_4^h for both models. Since the assumption of hydrostatic equilibrium is cen-

Table 7. Fundamental Eigenmodes of Mars

	Model A		Model B	
n	${}_0S_n$, s	${}_0T_n$, s	${}_0S_n$, s	${}_0T_n$, s
2	1775	1728	1918	1765
3	1109	1128	1211	1146
4	821	866	881	878
5	671	712	700	721
6	580	608	591	616
7	517	532	519	540
8	468	474	466	482
9	429	430	426	436
10	395	390	392	398

Note that a purely elastic mantle and a fluid core are assumed.

Table 8. Complex Dynamic Body Tide Love Numbers of Mars (Model A) With Reference to Phobos Tides

n	$\Re(h_n)$	$100 \times \Im(h_n)$	$\Re(k_n)$	$100 \times \Im(k_n)$	$\Re(l_n)$	$100 \times \Im(l_n)$
2	0.16928	-0.16957	0.09137	-0.09175	0.03519	-0.01731
3	0.08084	-0.03981	0.03002	-0.01463	0.00963	0.00132
4	0.05579	-0.01293	0.01586	-0.00361	0.00483	0.00078
5	0.04508	-0.00525	0.01037	-0.00118	0.00280	0.00033
6	0.03873	-0.00251	0.00748	-0.00047	0.00175	0.00015
7	0.03192	-0.00135	0.00568	-0.00022	0.00116	0.00008
8	0.03065	-0.00079	0.00447	-0.00011	0.00081	0.00004
9	0.02777	-0.00050	0.00360	-0.00006	0.00060	0.00003
10	0.02538	-0.00033	0.00296	-0.00004	0.00046	0.00002

Note that a viscoelastic mantle and a fluid core are assumed.

tral to the present study, the resultant topographic and gravitational oblatenesses should be identical. The difference in equatorial and polar radius and surface gravity is given by $a - c$ and $g_a - g_c$, respectively, whereas $C - A$ is the difference between principal polar and equatorial moments of inertia. The annual rate of spin–axis precession, ω_p defined as [*Esposito et al.*, 1992]

$$\omega_p = -\frac{3}{2}\frac{n_{rev}^2}{\Omega}\frac{J_2}{C/M_p r_p^2}\cos\psi \qquad (62)$$

where $\Omega = 2\pi/\tau_{rot}$ is the rotation rate, $n_{rev} = 2\pi/\tau_{rev}$ is the orbital mean motion, ψ is the obliquity of Mars, and $J_2 = 1960.454 \times 10^{-6}$ is the observed gravitational oblateness, is found to be -7.5 arc sec yr^{-1} (model A) and -7.7 arc sec yr^{-1} (model B), respectively. These values are in good agreement with the recent estimate of -7.85 $\pm$ 1.62 arc sec yr^{-1} based on a combination of astrometric observations of Phobos and Deimos, Viking lander range data, and Phobos 2 observations [*Sinclair and Morley*, 1992].

On a global scale the differences between both models are most obvious in the bulk iron-to-silicate ratio and in the dimensionless polar moment of inertia factor. The differences in the polar moment of inertia factor result in differences in the annual rate of spin–axis precession (see Table 10). The results suggest that the complex dynamic Love numbers of low harmonic degree of spherical representation indicative for Phobos–related tidal distortion of the Martian surface and the periods of low fundamental eigenmodes of free oscillation, in particular that of the gravest spheroidal mode ${}_0S_2$ roughly 30 min in duration, may have the potential to disentangle the gross interior structure of Mars (see Tables 7 through 9).

Nature and State of the Martian Crust and Lithosphere

In the absence of reliable seismic measurements of crust thickness, gravity and topography data are used to estimate the mean thickness of the Martian crust. Contributions to gravity anomalies arise from lateral variations in density and surface topography and from undulations of the crust–mantle boundary [*Bills and Ferrari*, 1978; *Kiefer et al.*, 1996]. Provided that the relatively low gravity anomalies observed in large areas of the northern lowlands and southern highlands (with the exception of Tharsis) can be interpreted in terms of Airy–type isostatic compensation of the global crustal dichotomy, a global mean crustal thickness of about 100 km has been inferred [*Janle*, 1983]. This corresponds to a crust volume normalized to planetary

Table 9. Complex Dynamic Body Tide Love Numbers of Mars (Model B) With Reference to Phobos Tides

n	$\Re(h_n)$	$100 \times \Im(h_n)$	$\Re(k_n)$	$100 \times \Im(k_n)$	$\Re(l_n)$	$100 \times \Im(l_n)$
2	0.20960	-0.20513	0.11190	-0.11059	0.03765	-0.02297
3	0.09384	-0.05152	0.03383	-0.01865	0.00862	0.00171
4	0.05945	-0.01686	0.01619	-0.00458	0.00457	0.00114
5	0.04581	-0.00669	0.01002	-0.00145	0.00292	0.00049
6	0.03867	-0.00304	0.00705	-0.00055	0.00198	0.00022
7	0.03405	-0.00153	0.00532	-0.00024	0.00141	0.00011
8	0.03066	-0.00083	0.00418	-0.00011	0.00104	0.00005
9	0.02801	-0.00047	0.00339	-0.00006	0.00080	0.00003
10	0.02585	-0.00028	0.00280	-0.00003	0.00064	0.00002

Note that a viscoelastic mantle and a fluid core are assumed.

Table 10. Physical Properties of Mars

	Model A	Model B
Global Properties		
Bulk iron-to-silicate ratio Fe/Si	1.35	1.71
Secular Love number k_2^f	1.207	1.130
Geometric flattening $10^2 \times (a-c)/a$	0.5059	0.4879
Gravitational flattening $10^2 \times (g_a - g_c)/g_a$	0.6404	0.6580
Dynamic flattening $10^2 \times (C-A)/C$	0.5035	0.4837
Dimensionless polar moment of inertia factor $C/M_p r_p^2$	0.3663	0.3566
Dimensionless equatorial moment of inertia factor $A/M_p r_p^2$	0.3645	0.3549
$10^2 \times J_2^h$	0.1844	0.1725
$10^5 \times J_4^h$	−0.7185	−0.6227
Annual rate of spin–axis precession ω_p, arc sec yr^{-1}	7.5	7.7
Global dissipation function Q_{gl}	99.6	101.2
Crust and Mantle		
Mantle Rayleigh number Ra	9.9×10^4	2.2×10^4
Mantle Nusselt number Nu	10.6	6.46
Mantle depletion factor ξ_m	0.155	0.360
Mantle activation parameter a^*	33.525	36.500
Crustal heat source skin depth h_e, km	31.5	66.9
Mantle Urey ratio	0.963	0.929
Crust Urey ratio	0.396	0.668
Flexural rigidity of rheological lithosphere D, 10^{26} N m	5.48	7.61

volume [*Esposito et al.*, 1992] of more than 10 times that of the Earth. The mineralogy of the SNCs and ALH84001 may provide additional clues to the thickness of the crust. While ALH84001 does not allow an absolute crust thickness estimate for the ancient southern hemisphere, since it is a cumulate rock, its composition of 96% orthopyroxene suggests a high degree of partial melting and thus a large crust volume. The crystallization age of the orthopyroxene is 4.6 Gyr, suggesting that the southern hemisphere crust, which may extend underneath the basaltic crust into the northern hemisphere, formed very early, as in the early differentiation model of *Breuer et al.* [1993]. These authors argue that the limits on crust volume from ^{40}Ar data [*Dreibus and Wänke*, 1987] apply only to the secondary basaltic northern hemisphere crust to suggest a mean thickness for that crust layer of 35 km. The total thickness of the crust may be much larger even globally if the ancient pyroxene rich crust extends into the northern hemisphere underneath the basaltic crust. If Pratt–type compensation is assumed, the elevation of the highland–lowland escarpment of 1-2 km between both hemispheres implies a difference in crust thickness between the two hemispheres of 10 to 20 km [*Janle*, 1983]. A mean crustal thickness estimate based on the interpretation of gravity data suffers from uniqueness problems inherent in any interpretation of the gravity field. If the crust thicknesses of the present models are considered large, it must be pointed out that thinner crusts can only be obtained if the crustal STP density is reduced. For instance, additional calculations have shown that model A of the present study yields crust thicknesses ranging from 50 km up to 200 km, when the crust density is varied between 2600 kg m^{-3} typical of regolith and 3200 kg m^{-3} representative of basaltic rock. At the crust–mantle boundary, accordingly, the pressure ranges from 0.5 to 2 GPa and temperatures vary between 400 and 1300 K. Under these circumstances, the critical depth of eclogitization could be reached in the lower crust. This may limit crust growth by way of delamination of the dense eclogite lower crust layer.

Using a Pratt type isostatic compensation model for the Tharsis rise and assuming that the base of the lithosphere coincides with the critical depth of stress compensation, *Sleep and Phillips* [1979] obtained a regional lithospheric thickness estimate of more than 300 km. A variety of subsequent studies using elastic flexure theory challenged the conclusion that local features such as large single volcanic loads accompanied by circumferential narrow grabens would require rheological lithosphere thicknesses between 20 and 60 km. Topographic features on a regional scale such as Olympus Mons, Elysium Planitia, and Isidis Basin, however, appear to imply lithospheres being from 100 up to 400 km in thickness [*Solomon and Head*, 1982; *Janle and Meissner*, 1986]. On a global scale the rheological lithosphere thickness has been concluded to be greater than 150 km. However, it should be kept in mind that these thickness estimates are restricted to the time of load emplacement and graben formation, thereby imposing some additional constraints on the thermal history a specific surface feature may have undergone [*Banerdt et al.*, 1992]. In any case a mean rheological lithospheric thickness of about 300 km as obtained with models A and B may be considered as a plausible value, reflecting the present thermal state of the planet. Thermal evolution calculations actually suggest the present rheological lithosphere of Mars to be some 100 km thick, depending on the true amount of volcanic heat advection during the early stages of evolution [*Schubert and Spohn*, 1990; *Spohn*, 1991; *Schubert et al.*, 1992]. Using a two stage evolution model of the formation of the global crustal dichotomy of Mars through mantle differentiation, *Breuer et al.* [1993] have found lithospheric thicknesses in the 150- to 250-km range beneath the northern lowlands, depending on the amount of thermal blanketing attributed to the ancient southern highland crust.

As a measure for the ability to withstand viscoelastic relaxation over a geologic timescale when being subjected to topographic loads, we calculate the effective flexural rigidity D of the rheological lithosphere according to [e.g., *Janle and Meissner*, 1986]

$$D = \frac{\bar{E} d_{\mathrm{rheo}}^3}{12(1-\bar{\nu}^2)} \tag{63}$$

where $\bar{E}$ and $\bar{\nu}$ is Young's modulus and Poisson's ratio as averaged across the entire vertical extent $d_{\mathrm{rheo}} = r_p - r_{\mathrm{rheo}}$ of the rheological lithosphere. It should be noticed, however, that D generally is believed to be age-dependent, in that it depends on the time when topographic loads such as polar ice sheets or volcanic constructs were placed onto the Martian surface [*Janle and Meissner*, 1986]. Hence the resultant present-day flexural rigidity ranging from 5.5×10^{26} (model A) to 7.5×10^{26} N m (model B) as listed in Table 10 is to be considered as an upper limit when compared to results reached solely on grounds of geologic arguments.

The cold thermal boundary layer of mantle convection underneath the lithosphere is found to be 150 to 200 km thick, resulting in a mean thermal lithosphere thickness of about 500 km. This corresponds to a surface heat flow density of 25 to 30 mW m^{-2} which compares well with thermal evolution models, some accounting for mantle differentiation and crust formation, which give present-day heat flow values in the range between 10 and 40 mW m^{-2} [*Stevenson et al.*, 1983; *Spohn*, 1991; *Breuer et al.*, 1993]. Since model B requires the formation of a relatively thick crust layer, the mantle is much more depleted in its radioactive heat source inventory as compared with model A. As a consequence, the skin depth h_e as the depth for crustal heat production to decrease by a factor of e is by a factor of 2 larger in model B than in model A. An estimate of the bulk contribution of crustal heat production to the surface heat flow q_p is provided by the crust Urey ratio [*Breuer et al.*, 1993]

$$U_{\mathrm{cr}} = 1 - \frac{q_{\mathrm{cr}}}{q_p}\left(\frac{r_{\mathrm{cr}}}{r_p}\right)^2 \tag{64}$$

where q_{cr} is heat flow density at the crust–mantle boundary with radius r_{cr}. In model B the crustal heat production accounts for about 70% of q_p, while the model A crust produces only 40% of the surface heat flow.

Nature and State of the Martian Mantle

There is considerable evidence that SNC meteorites and ALH84001 represent igneous crustal rocks extracted by partial melting from the uppermost Martian mantle and unaltered by weathering processes subsequent to surface emplacement. Hence SNC meteorites provide the most reliable means to constrain the mineralogic composition, oxidation state, and volatile content of the present Martian mantle. In terms of the major volatile–free minerals, the upper mantle has been concluded to contain about 50 wt% olivine, 30 wt% low–calcium orthopyroxene, 20 wt% high–calcium clinopyroxene, and minor aluminous phases such as low pressure plagioclase, which is replaced by spinel and garnet one after another until the critical depth of eclogitization somewhere in the 1 to 2 GPa pressure range is reached, thereby imposing an upper limit of 150 to 200 km to the Martian crust thickness [*Zharkov et al.*, 1991; *Longhi et al.*, 1992]. The distinct depletion of SNC meteorites in chalcophile elements supports the view of an homogeneous accretion of Mars. Therefore the Martian mantle must have experienced extensive early degassing and hydrogen escape following the equilibration of water with metallic iron. The latter would have resulted in a comparatively dry silicate mantle highly oxidized and particularly rich in FeO [*Wänke and Dreibus*, 1988; *Wänke*, 1991]. It has been proposed that considerable amounts of hydrogen might be dissolved in the iron phase, thereby reducing density and melting temperature of the Martian core far beyond that which would be expected for a sulfur–rich Fe-Ni–FeS core [*Zharkov et al.*, 1991]. In addition, such an accretion history offers an explanation for the FeO–rich compositions of the SNC magma source regions and for the geologic evidence for lava flows several hundreds of kilometers long. The lava must have had an extremely low viscosity that may have been due to high FeO contents [*McGetchin and Smyth*, 1978; *McSween*, 1985].

As all other models of sufficient detail, our models show that the Martian mantle is subdivided into a lower spinel mantle and an upper olivine mantle. In our models the transition occurs at a relative radius 0.7 and is accompanied by a 10% density increase. The β-spinel–γ-spinel transition is located at a relative radius 0.6 considerably above the planet's core-mantle boundary. These transitions occur at a greater depth than in the Earth's mantle simply because of the lower pressures in the Martian mantle. The smaller pressure gradient will have the additional consequence that the transitions will be spread over a wider depth range. Hence the mantle phase transition region of Mars is probably marked by two exothermic phase transformations above the core-mantle boundary, thereby providing a highly efficient acceleration mechanism for vertical mantle flow sufficient for locally elevated viscous dissipation and partial melt generation [*Zhou et al.*, 1995; *Breuer et al.*, 1996]. In the presence of the endothermic phase transition from spinel to perovskite the planform of mantle convection would be dominated by a single-plume pattern, which could offer an explanation for the concentration of volcanic activity on the Tharsis Province and its nonhydostatic contribution to the Martian gravity field [H. Harder, Phase transitions and the 3D-planform of thermal convection in the Martian mantle, submitted to *Journal of Geophysical Research*, 1996; *Harder and Christensen*, 1996]. As indicated by recent experimental studies, the possible existence of a perovskite layer and its stable phase assemblage at the base of the mantle not only depends on the core-mantle boundary pressure, i.e., the size and composition of the core, but is also very sensitive to the temperature distribution of the Martian interior [*Bertka and Fei*, 1996a]. In both models A and B of the present study, pressure and temperature in the mantle are not sufficient for the spinel–perovskite transition to occur in the 22 to 24 GPa range [*Leliwa-Kopystyński and Bakun-Czubarow*, 1980; *Chopelas et al.*, 1994]. If the core were solid, however,

experimentally determined structural changes of solid iron sulfide at Martian core pressures and temperatures would imply a significant reduction in core size. *Fei et al.* [1995] suggest that a lower mantle perovskite layer of significant thickness could be present under these circumstances. We have used their parameter values and found for model A the marginal possibility for a very thin (several ten kilometers) perovskite layer. For model B, however, a perovskite layer could not be obtained under these circumstances.

A number of previous studies have already shown that the mean mantle density would be rather insensitive to the composition and size of the metallic core given a fixed value for the dimensionless moment of inertia factor [*Johnston et al.*, 1974; *Göttel*, 1981; *Schubert and Spohn*, 1990; *Schubert et al.*, 1992]. Thus a reliable determination of the polar moment of inertia factor by a precise measurement of the spin–axis precession period according to (62) will provide excellent means to constrain the mantle density and thereby the FeO content of the Martian mantle. The principal insensibility of the mantle density to core chemistry may further imply an interpretation of the deep seismic velocity structure if obtained from inversions of body wave traveltime curves from future seismology missions in terms of the chemical composition of the mantle. Therefore future measurements of the spin–axis precession period together with the seismic wave velocities will enable one to test the correctness of the SNC hypothesis. Moreover, the inversion of periods of eigenmodes measured at the surface of Mars may impose additional constraints on the gross planetary structure as well as on the radial distribution of seismic attenuation, and hence mantle viscosity. While the current consensus is that the attenuation of seismic energy in the Martian mantle will play an important role, the level of seismic activity of Mars sufficient for the excitation of free oscillations is still subject to considerable uncertainty [e.g., *Lognonné and Mosser*, 1993].

Size and State of the Martian Core

The apparent absence of a dynamo-driven magnetic field, in spite of Mars' appreciable core size and rapid rotation, has often been contended to indicate either a solid state of the core or a completely molten core devoid of intrinsic heat sources necessary to drive sufficiently vigorous thermal convection. Recent thermal history calculations by *Schubert and Spohn* [1990] suggest that the latter would require an initial core sulfur content of at least about 15 wt% if the mantle viscosity is in the 10^{16} to 5×10^{16} m^2 s^{-1} range. For smaller initial sulfur concentrations, an inner core would freeze out and the continuous release of latent heat and gravitational energy would be sufficient to drive a dynamo with a substantial field at present. It has also been suggested, however, that the shielding effect of the iron–rich Martian mantle along with the relatively small size of the Martian core when compared to that of the Earth and the reduced electric conductivity of a sulfur–rich core alloy could frustrate the operation of a self–sustained dynamo [*Anderson*, 1972].

Seismological observations at the surface of Mars may be expected to place the most reliable constraints on the physical state and the chemical composition of the Martian core. Given that there are Marsquakes sufficiently large to excite low harmonic free oscillations of the planet, *Okal and Anderson* [1978] show that the period of the gravest spheroidal mode ${}_0S_2$ in case of a solid core would be roughly 2/3 of that in the presence of a completely molten core, as suggested by the present study. Further indicators of a liquid core or core shell would be the existence and the lateral extent of a seismic shadow zone and the amplitudes of core–reflected phases of nearly vertically incident seismic waves that would be greatly affected.

Concluding Remarks

Provided SNC meteorites are igneous crustal rocks ejected from the surface of Mars in the past history of the planet, the model calculations suggest molten Fe-Ni–FeS cores with radii a little less than one half of the planetary radius which are surrounded by silicate mantles subdivided into lower spinel layers and upper olivine layers and overlain by 100- to 250-km-thick basaltic crusts with surface heat flow densities in the 25 to 30 mW m^{-2} range. While the spinel layers should be again subdivided into β- and γ-spinel layers, the pressure in the mantle is found to be not sufficient for the spinel to perovskite transition to occur.

An improved knowledge of the Martian interior clearly necessitates the future deployment of a planetwide network consisting of several surface stations carrying those geophysical experiments which are capable of resolving the gross interior structure of Mars in terms of the mean thickness of the basaltic crust; the location of possible mantle discontinuities such as the α-olivine–β-spinel and β-spinel–γ-spinel transitions; and the size and physical state of the Martian core. In the absence of reliable measurements of the spin–axis precession period and seismological data, theoretical studies such as the present one are necessarily limited by the principal nonuniqueness introduced by certain assumptions regarding the nonhydrostatic contributions to the oblateness of the Martian gravity field and the bulk chemical composition of the planet. In particular, the parameterization of the equation of state for planetary materials as well as the depth distributions of crustal heat sources and mantle viscosity represent a further source of principal uncertainty for this kind of planetary modeling. Thus the most obvious discrepancy in crust thickness and core size between the two end–member type models of Mars' present interior structure, each of them either consistent with the geochemical or geophysical requirement, respectively, may at least partly reflect these circumstances.

Acknowledgments. We have benefited from helpful discussions with Doris Breuer, Gerlind Dreibus-Kapp, Peter Janle, and Heinrich Wänke. We are grateful to Constance Bertka and Helmut Harder, who provided preprints of their work. We thank John Longhi and Norman Sleep for valuable comments on the manuscript. Frank Sohl acknowl-

edges a postgraduate research grant from the University of Kiel and the Land Schleswig-Holstein. The manuscript was completed during a postdoctoral research grant from the Deutsche Forschungsgemeinschaft. The figures were produced by using the freely distributed GMT software package [*Wessel and Smith*, 1991]. Contribution No. 585 Institut für Geophysik, Universität Kiel.

References

Ahrens, T. J., Equations of state of iron sulfide and constraints on the sulfur content of the Earth, *J. Geophys. Res.*, *84*, 985–998, 1979.

Akaogi, M., E. Ito, and A. Navrotsky, Olivine-modified spinel–spinel transitions in the system Mg_2SiO_4–Fe_2SiO_4: Calorimetric measurements, thermochemical calculation, and geophysical application, *J. Geophys. Res.*, *94*, 15,671–15,685, 1989.

Anderson, D. L., Internal constitution of Mars, *J. Geophys. Res.*, *77*, 789–795, 1972.

Anderson, D. L., *Theory of the Earth*. Blackwell Sci., Cambridge, Mass., 1989.

Anderson, O. L., D. G. Isaak, and H. Oda, High-temperature elastic constant data on minerals relevant to geophysics, *Rev. Geophys.*, *30*, 57–90, 1992.

Anderson, O. L., K. Masuda, and D. G. Isaak, A new thermodynamic approach for high pressure physics, *Phys. Earth Planet. Inter.*, *91*, 3–16, 1995.

Ash, R. D., S. F. Knott, and G. Turner, A 4-Gyr shock age for a martian meteorite and implications for the cratering history of Mars, *Nature*, *380*, 57–59, 1996.

Babeyko, A. Y., S. V. Sobolev, and V. N. Zharkov, On mineralogical and velocity structure of the Martian crust, *Astron. Vestn.*, *27*(2), 55–75, 1993.

Balmino, G., G. Moynot, and N. Valés, Gravity field model of Mars in spherical harmonics up to degree and order eighteen, *J. Geophys. Res.*, *87*, 9735–9746, 1982.

Banerdt, W. B., M. P. Golombek, and K. L. Tanaka, Stress and tectonics on Mars, in *Mars*, edited by H. H. Kieffer, B. M. Jakosky, C. W. Snyder, and M. S. Matthews, pp. 249–297. Univ. of Ariz. Press, Tucson, 1992.

Bertka, C. M., and Y. Fei, Mineralogy of the Martian interior up to core-mantle boundary pressures, *J. Geophys. Res.*, in press, 1996a.

Bertka, C. M., and Y. Fei, A profile of Martian mantle mineralogy and density up to core-mantle boundary pressures, *Lunar Planet. Sci. Conf.*, *27*, 107–108, 1996b.

Bills, B. G., The moments of inertia of Mars, *Geophys. Res. Lett.*, *16*, 385–388, 1989.

Bills, B. G., and A. J. Ferrari, Mars topography harmonics and geophysical implications, *J. Geophys. Res.*, *83*, 3497–3508, 1978.

Bina, C. R., and G. R. Helffrich, Calculation of elastic properties from thermodynamic equation of state principles, *Annu. Rev. Earth Planet. Sci.*, *20*, 527–552, 1992.

Binder, A. B., Internal structure of Mars, *Phys. Earth Planet. Inter.*, *74*, 3110–3118, 1969.

Binder, A. B., and D. R. Davis, Internal structure of Mars, *Phys. Earth Planet. Inter.*, *7*, 477–485, 1973.

Boehler, R., The phase diagram of iron to 430 kbar, *Geophys. Res. Lett.*, *13*, 1153–1156, 1986.

Boehler, R., N. von Bargen, and A. Chopelas, Melting, thermal expansion, and phase transitions of iron at high pressures, *J. Geophys. Res.*, *95*, 21,731–21,736, 1990.

Born, G. H., Mars physical parameters as determined from Mariner 9 observations of the natural satellites and Doppler tracking, *J. Geophys. Res.*, *79*, 4837–4844, 1974.

Breuer, D., T. Spohn, and U. Wüllner, Mantle differentiation and the crustal dichotomy of Mars, *Planet. Space Sci.*, *41*, 269–283, 1993.

Breuer, D., H. Zhou, D. A. Yuen, and T. Spohn, Phase transitions in the Martian mantle: Implications for the planet's volcanic history, *J. Geophys. Res.*, *101*, 7531–7542, 1996.

Burns, J. A., Contradictory clues as to the origin of the Martian moons, in *Mars*, edited by H. H. Kieffer, B. M. Jakosky, C. W. Snyder, and M. S. Matthews, pp. 1283–1301. Univ. of Ariz. Press, Tucson, 1992.

Carr, M. H., and H. Wänke, Earth and Mars: Water inventories as clues to accretional histories, *Icarus*, *98*, 61–71, 1992.

Chopelas, A., R. Boehler, and T. Ko, Thermodynamics and behavior of γ-Mg_2SiO_4 at high pressure: Implications for Mg_2SiO_4 phase equilibrium, *Phys. Chem. Min.*, *21*, 351–359, 1994.

Christensen, U. R., Mantle rheology, constitution, and convection, in *Mantle Convection: Plate Tectonics and Global Dynamics*, edited by W. R. Peltier, pp. 595–655. Gordon and Breach, New York, 1989.

Cook, A. H., The moment of inertia of Mars and the existence of a core, *Geophys. J. R. Astron. Soc.*, *51*, 349–356, 1977.

Dreibus, G., and H. Wänke, Mars: A volatile rich planet, *Meteoritics*, *20*, 367–382, 1985.

Dreibus, G., and H. Wänke, Volatiles on Earth and Mars: A comparison, *Icarus*, *71*, 225–240, 1987.

Esposito, P. B., W. B. Banerdt, G. F. Lindal, W. L. Sjogren, M. A. Slade, B. G. Bills, D. E. Smith, and G. Balmino, Gravity and topography, in *Mars*, edited by H. H. Kieffer, B. M. Jakosky, C. W. Snyder, and M. S. Matthews, pp. 209–248. Univ. of Ariz. Press, Tucson, 1992.

Fei, Y., C. T. Prewitt, H. K. Mao, and C. M. Bertka, Structure and density of FeS at high pressure and high temperature and the internal structure of Mars, *Science*, *268*, 1892–1894, 1995.

Göttel, K. A., Density of the mantle of Mars, *Geophys. Res. Lett.*, *8*, 497–500, 1981.

Gudkova, T. V., V. N. Zharkov, and S. A. Lebedev, The theoretical spectrum of free oscillations of Mars, *Astron. Vestn.*, *27*(2), 33–54, 1993.

Harder, H., and U. R. Christensen, A one-plume model of martian mantle convection, *Nature*, *380*, 507–509, 1996.

Hofmeister, A. M., Pressure derivatives of the bulk modulus, *J. Geophys. Res.*, *96*, 21,893–21,907, 1991.

Janle, P., Bouguer gravity profiles across the highland–lowland escarpment on Mars, *Earth Moon Planets*, *28*, 55–67, 1983.

Janle, P., and R. Meissner, Structure and evolution of the terrestrial planets, *Surv. Geophys.*, *8*, 107–186, 1986.

Jarvis, G. T., and W. R. Peltier, Convection models and geophysical observations, in *Mantle Convection: Plate Tectonics and Global Dynamics*, edited by W. R. Peltier, pp. 479–593. Gordon and Breach, New York, 1989.

Johnston, D. H., and M. N. Toksöz, Internal structure and properties of Mars, *Icarus*, *32*, 73–84, 1977.

Johnston, D. H., T. R. McGetchin, and M. N. Toksöz, The thermal state and internal structure of Mars, *J. Geophys. Res.*, *79*, 3959–3971, 1974.

Kamaya, N., F. Ohtani, T. Kato, and K. Onuma, High pressure phase transitions in a homogeneous model Martian mantle, in *Evolution of the Earth and Planets*, edited by E. Takahashi, R. Jeanloz, and D. Rubie, vol. 74 of *Geophys. Monogr. Ser.*, pp. 19–25. AGU, Washington, D.C., 1993.

Kaula, W. M., The moment of inertia of Mars, *Geophys. Res. Lett.*, *6*, 194–196, 1979.

Kiefer, W. S., B. G. Bills, R. S. Nerem, and M. T. Zuber, An inversion of gravity and topography for mantle and crustal structure on Mars, *J. Geophys. Res.*, *101*, 9239–9252, 1996.

Kieffer, H. H., B. M. Jakosky, and C. W. Snyder, The planet Mars: From antiquity to the present, in *Mars*, edited by H. H. Kieffer, B. M. Jakosky, C. W. Snyder, and M. S. Matthews, pp. 1–33. Univ. of Ariz. Press, Tucson, 1992.

Leliwa-Kopystyński, J., and N. Bakun-Czubarow, The effect of material parameters on the shape of the phase separation surfaces within the Earth's mantle, *Phys. Earth Planet. Inter.*, *22*, 244–254, 1980.

Lognonné, P., and B. Mosser, Planetary seismology, *Surv. Geophys.*, *14*, 239–302, 1993.

Longhi, J., E. Knittle, J. R. Holloway, and H. Wänke, The bulk composition, mineralogy and internal structure of Mars, in *Mars*, edited by H. H. Kieffer, B. M. Jakosky, C. W. Snyder, and M. S. Matthews, pp. 184–208. Univ. of Ariz. Press, Tucson, 1992.

Mao, H. K., Y. Wu, L. C. Chen, J. F. Shu, and A. P. Jephcoat, Static compression of iron to 300 GPa and $Fe_{0.8}Ni_{0.2}$ alloy to 260 GPa: Implications for composition of the core, *J. Geophys. Res.*, *95*, 21,737–21,742, 1990.

McGetchin, T. R., and J. R. Smyth, The mantle of Mars: Some possible geological implications of its high density, *Icarus*, *34*, 512–536, 1978.

McKenzie, D., and M. J. Bickle, The volume and composition of melt generated by extension of the lithosphere, *J. Petrol.*, *26*, 625–679, 1988.

McSween, H. Y., SNC meteorites: Clues to Martian petrologic evolution?, *Rev. Geophys.*, *23*, 391–416, 1985.

McSween, H. Y., What we have learned about Mars from SNC meteorites, *Meteoritics*, *29*, 757–779, 1994.

Meissner, R. O., and U. R. Vetter, Relationship between the seismic quality factor Q and the effective viscosity η^*, *J. Geophys.*, *45*, 147–158, 1979.

Mittlefehldt, D. W., ALH84001, a cumulate orthopyroxenite member of the martian meteorite clan, *Meteoritics*, *29*, 214–221, 1994.

Morgan, J. W., and E. Anders, Chemical composition of Mars, *Geochim. Cosmochim. Acta*, *43*, 1601–1610, 1979.

Munk, W. H., and G. J. F. MacDonald, *The Rotation of the Earth: A Geophysical Discussion*. Cambridge Univ. Press, New York, 1975.

Ohtani, E., and N. Kamaya, The geochemical model of Mars: An estimation from the high pressure experiments, *Geophys. Res. Lett.*, *19*, 2239–2242, 1992.

Okal, E. A., and D. L. Anderson, Theoretical models for Mars and their seismic properties, *Icarus*, *33*, 514–528, 1978.

Poirier, J. P., *Introduction to the Physics of the Earth's Interior*. Cambridge Univ. Press, New York, 1991.

Poirier, J. P., and R. C. Liebermann, On the activation volume for creep and its variation with depth in the Earth's lower mantle, *Phys. Earth Planet. Inter.*, *35*, 283–293, 1984.

Press, W. H., B. P. Flannery, S. A. Teukolsky, and W. T. Vetterling, *Numerical Recipes*. Cambridge Univ. Press, New York, 1992.

Ranalli, G., *Rheology of the Earth. Deformation and Flow Processes in Geophysics and Geodynamics*. Allen & Unwin, Winchester, Mass., 1987.

Reasenberg, R. D., The moment of inertia and isostasy of Mars, *J. Geophys. Res.*, *82*, 369–375, 1977.

Reynolds, R. T., and A. L. Summers, Calculations on the composition of the terrestrial planets, *J. Geophys. Res.*, *74*, 2494–2511, 1969.

Robie, R. A., B. S. Hemingway, and J. R. Fischer, Thermodynamic properties of minerals and related substances at 298.15 K and 1 bar (10^5 Pascals) pressure and at higher temperatures, *U.S. Geol. Surv. Bull.*, *1452*, 456 pp., 1978.

Sammis, C. G., J. C. Smith, and G. Schubert, A critical assessment of estimation methods for activation volume, *J. Geophys. Res.*, *86*, 10,707–10,718, 1981.

Schubert, G., and T. Spohn, Thermal history of Mars and the sulfur content of its core, *J. Geophys. Res.*, *95*, 14,095–14,104, 1990.

Schubert, G., S. C. Solomon, D. L. Turcotte, M. J. Drake, and N. H. Sleep, Origin and thermal evolution of Mars, in *Mars*, edited by H. H. Kieffer, B. M. Jakosky, C. W. Snyder, and M. S. Matthews, pp. 147–183. Univ. of Ariz. Press, Tucson, 1992.

Severova, E., Phase transitions in the Mars mantle, *Earth Moon Planets*, *56*, 83–91, 1992.

Shampine, L. F., and M. K. Gordon, *Computer Solution of Ordinary Differential Equations. The Initial Value Problem*. Freeman, San Francisco, Calif., 1975.

Sinclair, A. T., and T. A. Morley, The determination of the precession rate of Mars from Phobos and Deimos observations, *Astron. Astrophys.*, *262*, 326–328, 1992.

Sleep, N. H., and R. J. Phillips, An isostatic model of the Tharsis province, Mars, *Geophys. Res. Lett.*, *6*, 803–806, 1979.

Smith, B. K., and F. O. Carpenter, Transient creep in orthosilicates, *Phys. Earth Planet. Inter.*, *49*, 314–324, 1987.

Smith, J. C., and G. H. Born, Secular acceleration of Phobos and Q of Mars, *Icarus*, *27*, 51–53, 1976.

Solomon, S. C., and J. W. Head, Evolution of the Tharsis province of Mars: The importance of heterogeneous lithospheric thickness and volcanic construction, *J. Geophys. Res.*, *87*, 9755–9774, 1982.

Spohn, T., Mantle differentiation and thermal evolution of Mars, Mercury, and Venus, *Icarus*, *90*, 222–236, 1991.

Stacey, F. D., Applications of thermodynamics to fundamental Earth physics, *Geophys. Surv.*, *3*, 175–204, 1977.

Stacey, F. D., B. J. Brennan, and R. D. Irvine, Finite strain theories and comparisons with seismological data, *Geophys. Surv.*, *4*, 189–232, 1981.

Stevenson, D. J., T. Spohn, and G. Schubert, Magnetism and thermal evolution of the terrestrial planets, *Icarus*, *54*, 466–489, 1983.

Sumino, Y., and O. L. Anderson, Elastic constants of minerals, in *CRC Handbook of Physical Constants*, edited by R. S. Carmichael, vol. III, pp. 40–137. CRC Press, Boca Raton, Fla., 1984.

Surkov, Y. A., V. L. Barsukov, L. P. Moskaleva, V. P. Kharyukova, S. Y. Zaitseva, G. G. Smirnov, and O. S. Manvelyan, Determination of the elemental composition of Martian rocks from Phobos 2, *Nature*, *341*, 595–598, 1989.

Thomas, P. C., Planetary geodesy, U.S. Natl. Rep. Int. Geod. Geophys. 1987–1990, *Rev. Geophys.*, *29*, 182–187, 1991.

Toksöz, M. N., A. T. Hsui, and D. H. Johnston, Thermal evolutions of the terrestrial planets, *Earth Moon Planets*, *18*, 281–320, 1978.

Treiman, A. H., A petrographic history of martian meteorite ALH84001: Two shocks and an ancient age, *Meteoritics*, *30*, 294–302, 1995.

Turcotte, D. L., and G. Schubert, *Geodynamics*. John Wiley, New York, 1982.

Urey, H. C., *The Planets: Their Origin and Development*. Yale Univ. Press, New Haven, Conn., 1952.

Wänke, H., Chemistry, accretion, and evolution of Mars, *Space Sci. Rev.*, *56*, 1–8, 1991.

Wänke, H., and G. Dreibus, Chemical composition and accretion history of terrestrial planets, *Philos. Trans. R. Soc. London, Ser. A*, *325*, 545–557, 1988.

Watt, J. P., G. F. Davies, and R. J. O'Connell, The elastic properties of composite materials, *Rev. Geophys.*, *14*, 541–563, 1976.

Weertman, J., and J. R. Weertman, High temperature creep of rock and mantle viscosity, *Annu. Rev. Earth Planet. Sci.*, *3*, 293–315, 1975.

Wessel, P., and W. H. F. Smith, Free software helps map and display data, *Eos Trans. AGU*, *72*, 441,445–446, 1991.

Wood, J. A., et al., Geophysical and cosmochemical constraints on properties of mantles of the terrestrial planets, in *Basaltic Volcanism on the Terrestrial Planets*, edited by B. V. S. Project, pp. 633–699. Pergamon, New York, 1981.

Zharkov, V. N., and T. V. Gudkova, On the dissipation factor of Martian interiors, *Astron. Vestn.*, *27*(4), 3–15, 1993.

Zharkov, V. N., E. M. Koshlyakov, and K. I. Marchenkov, The composition, structure, and gravitational field of Mars, *Astron. Vestn.*, *25*(5), 515–547, 1991.

Zhou, H., D. Breuer, D. A. Yuen, and T. Spohn, Phase transitions in the Martian mantle and the generation of megaplumes, *Geophys. Res. Lett.*, *22*, 1945–1948, 1995.

F. Sohl and T. Spohn, Institut für Planetologie, Westfälische Wilhelms-Universität, Wilhelm-Klemm-Str. 10, D–48149 Münster, Germany. (email: sohl@uni-muenster.de; spohn@uni-muenster.de)

(Received May 7, 1996; revised October 9, 1996; accepted November 1, 1996.)